

ALMA MATER STUDIORUM · UNIVERSITÀ DI  
BOLOGNA

---

Scuola di Ingegneria e Architettura  
-Sede di Forlì-

**Influence of adhesive thickness on  
adhesively bonded joints under  
fatigue loading**

Aerospace Engineering Master Degree

Author:  
Nicola Zavatta

Supervisor:  
Prof. Enrico Troiani

Co-supervisors:  
Dr. Ir. René Alderliesten  
Ir. John-Alan Pascoe

Academic Year 2014/2015  
II Session



## Abstract

Research on adhesive joints is arousing increasing interest in aerospace industry. Incomplete knowledge of fatigue in adhesively bonded joints is a major obstacle to their application. The prediction of the disbonding growth is yet an open question. This thesis researches the influence of the adhesive thickness on fatigue disbond growth. Experimental testing on specimens with different thickness has been performed. Both a conventional approach based on the strain energy release rate and an approach based on cyclic strain energy are provided. The inadequacy of the former approach is discussed. Outcomes from tests support the idea of correlating the crack growth rate to the cyclic strain energy. In order to push further the study, a 2D finite element model for the prediction of disbond growth under quasi-static loading has been developed and implemented in *Abaqus*. Numerical simulations have been conducted with different values of the adhesive thickness. The results from tests and simulations are in accordance with each other. According to them, no dependence of disbonding on the adhesive thickness has been evidenced.



# Acknowledgements

This thesis has been possible thanks to the support received by some others. I would sincerely like to thank those people who made it possible to do research in Delft. Each of them allowed me to live a beautiful experience that goes well beyond the limits of a thesis. Dr. René Alderliesten accepted my request to do research at TU Delft, thus giving me this opportunity and, together with Ir. John-Alan Pascoe, suggested a suitable research topic. They were my supervisors in Delft and greatly contributed to the work contained in this thesis. Thank you Mr. Pascoe for your courtesy and for the help you gave me everyday in- and outside the lab. I would like to thank those, members of the technical staff, PhD students or professors, who somehow gave me an hand during the period at TU Delft.

Thank you Prof. Troiani for the support you have been giving me since the first time I asked you for a thesis project. Thank you for your advices, this thesis would not be the same without your contribution. Not only this, thank you Prof. for your friendliness and humanity.

Last but not least, I would like to thank a colleague, a friend with whom I shared much time, who has given his personal contribution to this work with an indefatigable pursuit of the errors scattered all through the thesis.

Vorrei poi spendere parole di ringraziamento verso tutti coloro che, pur non avendo contribuito tecnicamente alla presente tesi, mi hanno accompagnato durante la Laurea Magistrale.

In primo luogo grazie ai miei genitori, grazie Pa' e Gio', per essermi sempre stati vicini.

Grazie a mia nonna Renza, alla zia Elsa, alla Michi e a Robi, quei parenti su cui puoi sempre contare.

Grazie a Stefano e Nicolò, compagni di università e amici, con cui ho condiviso tanti momenti di studio e divertimento.

Grazie alla ormai storica compagnia di avventure, Andrea, Lorenzo, Michael, Marco, Zuzu, e grazie a tutti gli altri amici con cui ho stretto rapporti.

Grazie a tutti voi che siete stati presenti in questi anni e lo siete tuttora.



# Contents

<b>1</b>	<b>Introduction</b>	<b>1</b>
<b>2</b>	<b>Theoretical background</b>	<b>3</b>
2.1	Fracture and energy release . . . . .	3
2.2	Cyclic strain energy approach . . . . .	6
2.3	Standard methods for SERR computation . . . . .	10
<b>3</b>	<b>Experimental set-up</b>	<b>13</b>
3.1	Specimen preparation . . . . .	13
3.2	Experimental set-up and calibration . . . . .	18
3.3	Fatigue testing . . . . .	23
3.4	Quasi-static testing . . . . .	25
<b>4</b>	<b>Experimental results</b>	<b>27</b>
4.1	Crack length measurement in fatigue tests . . . . .	27
4.2	Crack length measurement in quasi-static tests . . . . .	31
4.3	Energy calculation in fatigue testing . . . . .	33
4.4	Energy calculation in quasi-static testing . . . . .	39
4.5	Crack growth rate as a function of SERR . . . . .	42
4.6	Crack growth rate related to cyclic energy . . . . .	45
4.7	Crack growth rate in quasi-static tests . . . . .	48
<b>5</b>	<b>Numerical simulations</b>	<b>51</b>
5.1	Introduction to Cohesive Zone Models . . . . .	51
5.2	Implementation of the numerical model . . . . .	55
5.3	Numerical results . . . . .	59
<b>6</b>	<b>Conclusions</b>	<b>65</b>
<b>A</b>	<b>Specimen data</b>	<b>67</b>



# List of Figures

2.1	Stress relieving about fracture surfaces (based on [6]) . . . . .	4
2.2	Schematic representation of monotonic and cyclic energy . . . . .	7
2.3	Nonlinear effects on load-displacement curve at different $R$ . . . . .	9
3.1	Dimensions of DCB specimens (Courtesy by John-Alan Pascoe, TU Delft) . . . . .	14
3.2	Measurement station with Zeiss Axiovert 40 MAT . . . . .	15
3.3	Location of measured points A, B, C . . . . .	16
3.4	Microscopic picture of aluminium-epoxy interface . . . . .	17
3.5	Specimens coated with typewriter correction fluid . . . . .	18
3.6	User/machine interface . . . . .	19
3.7	Mounting of the specimen on the machine . . . . .	20
3.8	Experimental set-up . . . . .	21
3.9	Load-displacement calibration curve of specimen G-010 . . . . .	22
3.10	Profile of the applied displacement . . . . .	24
4.1	Plot of the crack length against the number of cycles . . . . .	29
4.2	Crack growth rate against the number of cycles . . . . .	30
4.3	Crack length and crack growth rate in quasi-static conditions . . . . .	32
4.4	Cyclic energy trend from experimental data . . . . .	34
4.5	Total energy trend from experimental data . . . . .	35
4.6	Logarithmic plot of $\frac{dU_{cyc}}{dN}$ as a function of $N$ . . . . .	37
4.7	Logarithmic plot of $\frac{dU_{tot}}{dN}$ as a function of $N$ . . . . .	38
4.8	Load-displacement curve from experimental data . . . . .	40
4.9	Plot of the energy $U_t$ against time $t$ . . . . .	41
4.10	Semi-logarithmic plot of $\frac{dU}{dt}$ versus $t$ . . . . .	41
4.11	Logarithmic plot of $\frac{da}{dN}$ against the maximum SERR . . . . .	43
4.12	Logarithmic plot of the crack growth rate against $\Delta\sqrt{G}$ . . . . .	44
4.13	Logarithmic plot of $\frac{dA}{dN}$ against $\frac{dU_{cyc}}{dN}$ . . . . .	46
4.14	Logarithmic plot of $\frac{dA}{dN}$ against $\frac{dU_{tot}}{dN}$ . . . . .	47
4.15	Correlation between $\frac{dA}{dN}$ and $\frac{dU}{dt}$ . . . . .	49

4.16	Logarithmic plot of $\frac{da}{dt}$ against the SERR . . . . .	50
5.1	Plot of the linear traction-separation law . . . . .	54
5.2	Configurations considered for the development of the model . . . . .	56
5.3	Tie constraints between surfaces (image based on [7]) . . . . .	58
5.4	Effect of fracture energy on crack growth . . . . .	60
5.5	Effect of cohesive stiffness on the stress distribution . . . . .	61
5.6	Stress field, in case of high cohesive stiffness . . . . .	62
5.7	Stress field, in case of low cohesive stiffness . . . . .	63
A.1	Pictures from G-006 at different stations . . . . .	69
A.2	Pictures from H-008 at different stations . . . . .	70
A.3	Pictures from G-005 at different sections . . . . .	72

# List of Tables

3.1	Calibration results of the specimens used for fatigue testing . . .	23
3.2	Data concerning fatigue testing . . . . .	25
4.1	Values of the coefficients in equation (4.1) and $RMSE$ . . . . .	28
4.2	Coefficients in equation (4.3) and $RMSE$ . . . . .	31
4.3	Coefficients in the fitting curve of $U_{cyc}$ . . . . .	36
4.4	Coefficients in the fitting curve of $U_{tot}$ . . . . .	39
4.5	Coefficients in equation (4.9) . . . . .	42
4.6	Coefficients $C$ and $n$ provided in [4] . . . . .	45
4.7	Coefficients $C$ and $n$ computed according to tests . . . . .	48
5.1	Mechanical properties used in the model . . . . .	58
5.2	Elements on the main diagonal of matrix $\mathbf{K}$ . . . . .	59
A.1	Length, width and thickness of specimens from series G and H	73
A.2	Thickness of the adhesive layer of series G specimens . . . . .	74
A.3	Thickness of the adhesive layer of series H specimens . . . . .	75
A.4	Groups used for specimen selection . . . . .	76
A.5	Summary of the specimens employed in tests . . . . .	76



# Chapter 1

## Introduction

Adhesive joints have gained considerable interest in recent years. Their promise of significant weight reduction is inherently attractive to aerospace industry. Adhesive bonding also offers advantages in terms of fatigue life, since it does not require drilling holes into the material and appears as a natural solution for joints in composites. The application of adhesive joints is however hindered by our lack of understanding of fatigue disbonding behaviour. The incapability to predict fatigue fracture of adhesives has led to strict certifications, which basically limit the advantages of adhesive joints themselves.

The present thesis deals with the problem of predicting the disbonding behaviour of aluminum-epoxy joints. In particular the influence of adhesive thickness on disbonding has been researched. This work is composed of two main parts. The first part concerns an experimental study conducted at TU Delft under the supervision of Dr. Ir. R.C. Alderliesten and of Ir. J.A. Pascoe. The object was the experimental determination of disbond growth in specimens with different adhesive thickness. The second part concerns numerical simulations performed under the supervision of Prof. E. Troiani. Their objective was the development of a finite element model for disbonding prediction.

The work is structured as follows:

Chapter 2 is an introduction to the theoretical background concerning our study. In particular, concepts related to energy-based approaches to fatigue are introduced.

Chapter 3 describes the specimens used for testing and their preparation. The experimental set-up and the test procedures are then illustrated.

Chapter 4 shows the outcomes of fatigue and quasi-static tests and provides

an interpretation of the results.

Chapter 5 deals with numerical simulations. First the theory underlying the numerical model employed is presented, then the implementation of the model is described. Finally the results of the simulations are provided.

Chapter 6 is a conclusion to the study. The outcomes of previous chapters are summarised and a comparison between experimental and numerical results is drawn.

Appendix A provides detailed data concerning the specimens.

# Chapter 2

## Theoretical background

This chapter introduces the theoretical background upon which the thesis is based. Theory concerning the numerical model is dealt with in the corresponding chapter. Several approaches to the study of fracture have been developed over the years. To the scope of this study, disbonding is considered as a crack that propagates inside the adhesive. In the following energy-based approaches to fatigue are illustrated, assuming basic knowledge of fracture mechanics.

### 2.1 Fracture and energy release

We start considering a crack of length  $a$  embedded into a solid structure. When a crack is created into a solid, the stress field about the fracture is modified. In particular, the presence of the crack causes a relieving of the stresses in the region adjacent to the crack surfaces, as shown in Figure 2.1. The stresses are associated to the energy stored in the material, or *strain energy*, which is denoted by  $U$ . Unloading a region about the crack surfaces results in releasing the strain energy contained in that region. Thus, cracks are associated to energy release and any increase of the crack length causes more energy to be released. On the other hand the formation of cracks implies breaking bonds into the material, which requires a certain amount of energy.

Griffith pointed out that a balance must exist between the energy supplied and the energy absorbed. The original balance equation suggested by Griffith can be modified to take into account other sources of energy dissipation. Griffith developed his idea working with brittle materials, specifically glass; when ductile materials are considered, the high stresses around the crack tip tend to produce local plasticity. The plastic region requires energy for

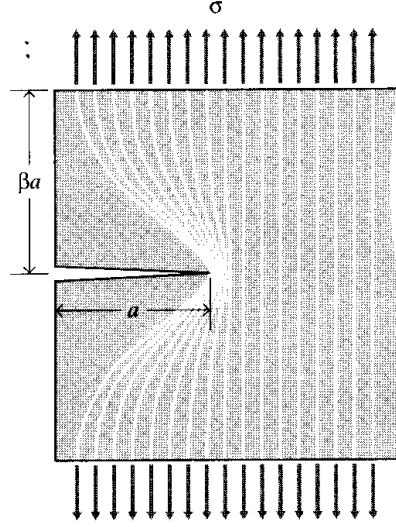


**Figure 2.1:** Stress relieving about fracture surfaces (based on [6])

its formation and is accounted as a mechanism of energy dissipation. The modified Griffith equation can be written as:

$$U = U_0 + U_a + U_\gamma + U_p - F, \quad (2.1)$$

where  $U$  is the strain energy in the cracked structure,  $U_0$  is the strain energy in the uncracked structure,  $U_a$  is the energy release discussed above,  $U_\gamma$  is the energy required for the formation of the crack,  $U_p$  is the energy dissipation due to plasticity and  $F$  is the work done by external forces. The terms responsible for energy dissipation can be summed together, yielding  $U_\gamma + U_p = W$ . Equation (2.1) can be differentiated with respect to the area of crack growth  $A$ , getting from an algebraic form to a differential one. Considering the derivative  $\frac{d}{dA}$  means evaluating the rate of change of the energy as the crack grows. Given that  $U_0$  is constant by definition, then  $\frac{dU_0}{dA} = 0$  and the equation becomes the following:

$$\frac{dU}{dA} = \frac{dU_a}{dA} + \frac{dW}{dA} - \frac{dF}{dA}. \quad (2.2)$$

If  $\frac{dU}{dA} < 0$  the strain energy decreases as the crack propagates. This situation corresponds to unstable cracking, because the structure tends to move towards a state of minimum energy. Thus, from equation (2.2), unstable crack growth occurs if:

$$\frac{d(F - U_a)}{dA} > \frac{dW}{dA}. \quad (2.3)$$

The left hand side is the energy supplied to the crack, driving crack growth. It is usually denoted by  $G$  and referred to as *strain energy release rate (SERR)*. The right hand side is the energy required per unit increase of crack length, denoted by  $G_c$ . It can be regarded as a critical value of SERR, beyond which unstable cracking occurs. In case of no work applied by external forces, (2.3) basically states that unstable crack growth occurs if the energy liberated by crack growth is greater than the energy dissipated throughout the process. This stability criterion is usually written in the form:

$$G > G_c. \quad (2.4)$$

Irwin derived an equation that relates the strain energy release rate to the stress intensity factor  $K$ , namely:

$$G = \frac{K^2}{E'}, \quad (2.5)$$

where  $E' = E$  in case of plane stress and  $E' = \frac{E}{1-\nu^2}$  in case of plain strain, being  $E$  the Young's modulus and  $\nu$  the Poisson's ratio. By means of equation (2.5) it is possible to express criterion (2.4) in terms of stress intensity factors, yielding

$$K > K_c. \quad (2.6)$$

The stress intensity factor  $K_c$  corresponding to the critical strain energy release rate  $G_c$  is called *fracture toughness*. It is usually considered a material parameter and is measured by testing. Inequality (2.6) is mainly used in metals, while in composites and adhesive bonds the use of  $G$  is preferred over that of  $K$ , due to the difficulty of estimating the stress intensity factor. Both the fracture toughness and the critical strain energy release rate depend on the fracture mode. This research study deals with Mode I fracture, also called opening mode. That occurs when a tensile stress is applied along the direction perpendicular to the plane of the crack. For sake of simplicity the subscript referring to Mode I will be omitted. The following notation is therefore implied throughout the entire thesis:  $G = G_I$ ,  $G_c = G_{Ic}$ ,  $K = K_I$  and  $K_c = K_{Ic}$ .

The findings illustrated so far hold for crack growth under quasi-static loading. In fatigue, in fact, crack growth occurs at values of the SERR significantly below the  $G_c$  computed in quasi-static tests. Paris' relation is usually employed to estimate crack growth in metals:

$$\frac{da}{dN} = C \Delta K^n. \quad (2.7)$$

Quantity  $\frac{da}{dN}$  is called *crack growth rate*. Coefficients  $C$  and  $n$  are determined empirically by curve fitting through experimental data. Modified versions of

Paris' law have been derived to express the dependence of the crack growth rate on the energy release rate. Among them:

$$\frac{da}{dN} = CG_{max}^n, \quad (2.8)$$

$$\frac{da}{dN} = C\Delta G^n, \quad (2.9)$$

where coefficients  $C$  and  $n$ , in general different, are computed by curve fitting.  $G_{max}$  is the maximum value of the SERR at each cycle, while the range  $\Delta G$  is the difference between the maximum and minimum  $G$  at each cycle. Much work concerning fatigue in composites or in adhesive bonds is based on modifications of Paris' relationship in which the role of  $\Delta K$  is taken on by some function of  $G$ , like (2.8) and (2.9). The use of  $\Delta\sqrt{G} = (\sqrt{G_{max}} - \sqrt{G_{min}})^2$  instead of  $\Delta G$  has been suggested, in order to preserve the similarity principle underlying (2.7). The problem with this approach is that the relations derived from Paris' law usually lack a physical basis. Many papers result in empirical relations that are nothing more but curve fittings and do not add much to our comprehension of fatigue. The question whether  $G_{max}$  or  $\Delta G$  or some other parameter should be most appropriate to characterise crack growth is rarely addressed. Actually the use of only one of these parameters to characterise load cycles is questionable. Considering, for instance, the maximum SERR, does not uniquely defines a cycle: infinite load cycles exist, which share the same value of  $G_{max}$ . In order to univocally determine each cycle, it is necessary to introduce an additional parameter. A common choice is the *R-ratio*  $R = \frac{P_{min}}{P_{max}}$ , i.e. the ratio between minimum and maximum load within the cycle. Since different load cycles produce different crack growth, the correlation curves obtained from the relationships above exhibit a dependence on  $R$ , known as *R-ratio effect*. Hence the need to find a quantity that characterises fatigue cycles in a unique way.

## 2.2 Cyclic strain energy approach

A promising approach has been proposed in [5]. The idea is looking into one single load cycle and determining the entire energy release during that cycle. Basically, an energy balance like the one used by Griffith should still hold in fatigue on the scale of a single cycle. A load-displacement curve is schematically represented in Figure 2.2. The values  $d_{min}$  and  $d_{max}$  are the minimum and maximum displacements encountered during a fatigue cycle<sup>1</sup>;

---

<sup>1</sup>The experimental tests discussed in this thesis have been conducted under displacement control, as explained in the next chapter.

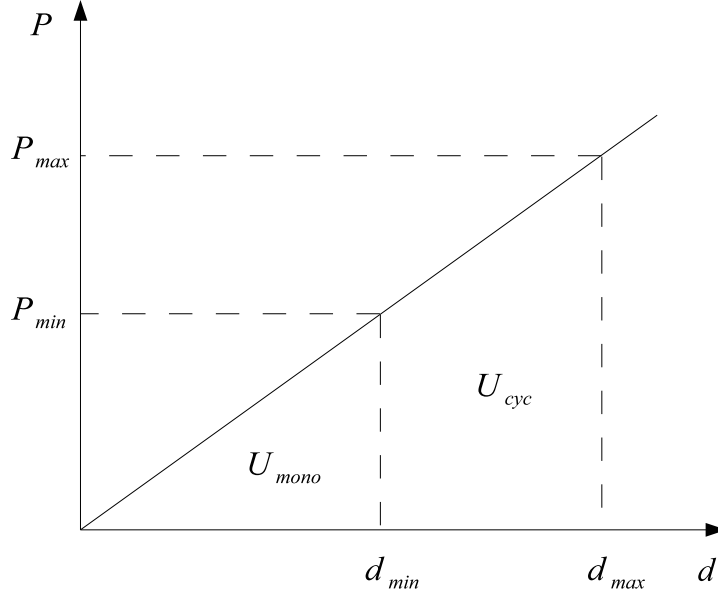


**Figure 2.2:** Schematic representation of monotonic and cyclic energy

the corresponding values of the force are  $P_{min}$  and  $P_{max}$ .

We define three components of the energy :

- the *monotonic energy*,  $U_{mono}$ , is the energy needed to reach the minimum displacement. This energy is supplied to the specimen used for testing at the beginning of the test and is not released until the specimen is brought back to the starting point;
- the *cyclic energy*,  $U_{cyc}$ , is the energy supplied to the specimens during each load cycle. It is represented by the area under the load-displacement line comprised between  $d_{min}$  and  $d_{max}$ . This energy is supplied to the specimen during the loading part of the cycle and is returned during the unloading part;
- the *total energy*, denoted by  $U_{tot}$ , is the sum of monotonic energy and cyclic energy.

The energy returned is actually less than that supplied, because of the dissipative mechanisms that take place into the specimen. This point will be discussed in further detail shortly.

The values of the energy can be computed easily under the hypothesis that the load-displacement curve is linear as shown in figure. In particular, the following expressions can be found:

$$U_{mono} = \frac{1}{2}P_{min}d_{min}, \quad (2.10)$$

$$U_{cyc} = \frac{1}{2}(P_{min} + P_{max})(d_{max} - d_{min}), \quad (2.11)$$

$$U_{tot} = \frac{1}{2}P_{max}d_{max}. \quad (2.12)$$

The actual trend of the load-displacement curve is not linear. The increase of crack length is responsible for a reduction of the elastic modulus, thus less and less force is required to attain the same displacement as the crack grows. Additionally, the formation of a plastic zone at the crack tip contributes to the decrease of stiffness; residual stresses are induced into the material and permanent deformation is left after the load is removed. Due to these mechanisms, the curve tends to be shifted downwards and zero force is attained at a non zero displacement. Both crack growth and plastic deformation absorb a certain amount of energy, acting like sinks. Therefore, part of the cyclic energy which is supplied during loading is dissipated throughout the cycle and is not returned during unloading. If testing is run under displacement control, i.e.  $d_{min}$  and  $d_{max}$  are fixed all through the test,  $U_{cyc}$  decreases continuously cycle after cycle. Involving the derivative with respect to the number of cycles  $N$ , we get  $\frac{dU_{cyc}}{dN} < 0$ .

Equations 2.10, 4.5 and 4.6 yield an error in the computation of the energy because nonlinear effects are neglected in their derivation. A qualitative estimate of this error can be got from Figure 2.3. Using equations above to compute the energy leads to overestimating the monotonic energy and to underestimating the cyclic energy. The overestimate of monotonic energy is equal to the area of triangle FEA, while the underestimate of cyclic energy is equal to the area of the region comprised between the curved line and segment AB. Figures 2.3a and 2.3b refer to cycles with different  $R$  (lower in the former). It can be noticed that the estimate error depends on the  $R$ -ratio. In particular, a high  $R$  causes a larger error in  $U_{mono}$  and a smaller error in  $U_{cyc}$ .

According to the idea discussed previously, the crack growth during one cycle is related to the energy release in that cycle. Derivatives  $\frac{dU_{cyc}}{dN}$  and  $\frac{dU_{tot}}{dN}$  can be regarded as the energy release per cycle. Similarly, the crack growth rate  $\frac{da}{dN}$  can be seen as the crack growth per unit cycle. In [5] the crack growth rate is correlated to both cyclic and total energy release through a power law, resulting in the following equations:

$$\frac{da}{dN} = C \left( \frac{dU_{cyc}}{dN} \right)^n, \quad (2.13)$$

$$\frac{da}{dN} = C \left( \frac{dU_{tot}}{dN} \right)^n. \quad (2.14)$$

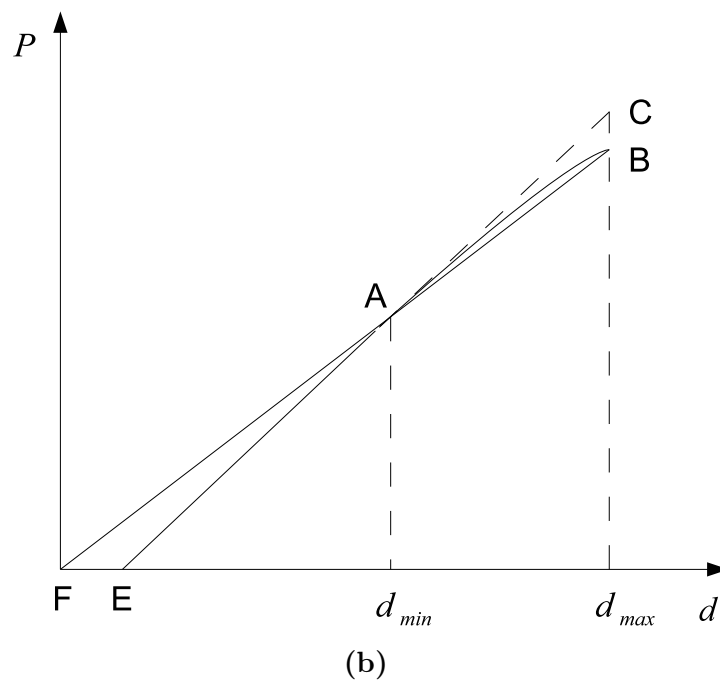
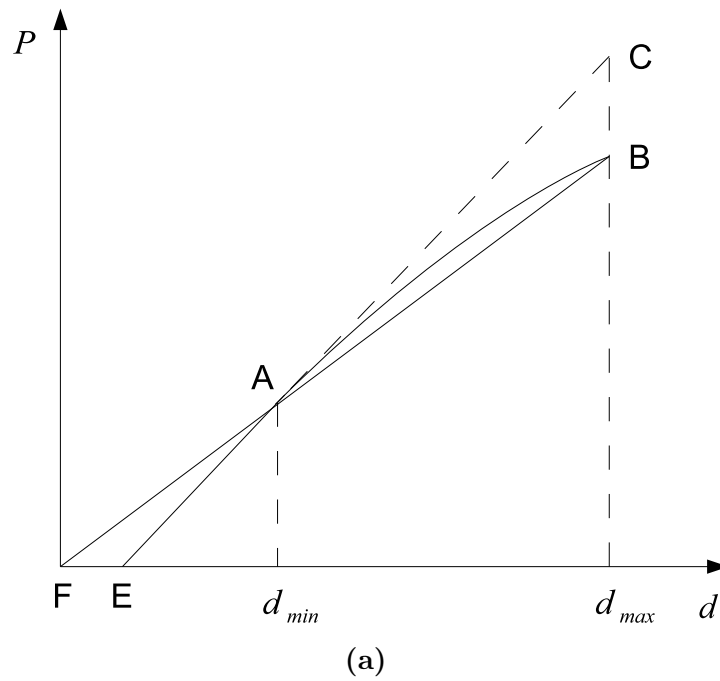


**Figure 2.3:** Nonlinear effects on load-displacement curve at different  $R$

Coefficients  $C$  and  $n$  are obtained by curve fitting through experimental data. The results from (2.13) and (2.14) will be dealt with extensively in chapter 4.

## 2.3 Standard methods for SERR computation

In this section we will briefly review the methods provided by ASTM Standard [1] for the computation of the Mode I strain energy release rate. This standard refers to displacement controlled quasi-static tests conducted on double cantilever beam *DCB* specimens (see next chapter for a detailed description). A visual measurement of the crack length is prescribed. Three methods are proposed for the determination of  $G$ :

- *Modified Beam Theory Method (MBT)*;
- *Compliance Calibration Method (CC)*;
- *Modified Compliance Calibration Method (MCC)*.

The MBT method is based on the expression for the strain energy release rate of a clamped double cantilever beam which results from beam theory. It is the following:

$$G = \frac{3Pd}{2wa}, \quad (2.15)$$

where  $P$  is the measured load,  $d$  is the displacement of the load point,  $w$  is the width of the specimen and  $a$  is the crack length. This method leads to a slight overestimate of  $G$  due to the fact that the beam is not perfectly built-in. A way to correct for this is considering an extended crack length  $a + \Delta$ , where  $\Delta$  is computed empirically as follows. Defining the compliance  $C = \frac{d}{P}$ , a plot of  $C^{\frac{1}{3}}$  versus  $a$  is obtained by least squares fitting through experimental data. The value  $\Delta$  is the distance between the origin and the point at which  $C^{\frac{1}{3}} = 0$ .

The CC method is based on the following formula:

$$G = \frac{nPd}{2wa}. \quad (2.16)$$

A least squares fitting of  $\log C$  against  $\log a$  is computed. Coefficient  $n$  is chosen as the slope of the straight line which results from the fitting.

The MCC method employs the following expression:

$$G = \frac{3(PC^{\frac{1}{3}})^2}{2Awh}, \quad (2.17)$$

where  $h$  is the thickness of the specimen and  $A$  is computed as follows. A least squares plot of  $\frac{a}{h}$  versus  $C^{\frac{1}{3}}$  is generated. The slope of the straight line resulting from the fitting is taken on as the value of  $A$ .

Results from (2.15), (2.16) and (2.15) are close one another and the deviation between them is estimated to be no more than 3.1%.



# Chapter 3

## Specimen preparation and experimental set-up

### 3.1 Specimen preparation

Tests have been performed on aluminium-epoxy double cantilever beam specimens. These specimens basically consist of two beams, usually with rectangular cross section, bonded together so to obtain a single piece. This type of specimen is quite popular in fatigue experiments, since it allows to easily create an artificial notch in correspondence of the junction surface between the two beams, thus resulting in a region of stress concentration and in a well-defined initial crack.

All the specimens employed during the tests were manufactured at the Delft Aerospace Structures and Materials Laboratory (*DASML*) according to the ASTM Standard D5528-01(07) [1], which regulates the testing of fibre-reinforced composite materials for the determination of Mode I interlaminar fracture toughness using DCB specimens. They were made out of two plates of 2024-T3 Aluminium alloy with a nominal thickness of 6 mm, bonded together with FM94 K.03AD FILM 915 epoxy adhesive, produced by Cytec. The aluminium was pre-treated by chromic acid anodisation and BR-127 primer was applied to the surface before bonding. In order to create an initial crack, some stripes of teflon tape were placed between the adherents at one side of the boundary to prevent adhesion. The plates were then cured in autoclave at a temperature of 120°C and a pressure of 6 bar for 1 hour. Both heating and cooling were performed using a ramp profile of the temperature, with a rate equal to 2°C/min. After the curing process the plates were milled into smaller parts to obtain specimens with the desired dimensions. ASTM Standard prescribes for the specimen a length greater or

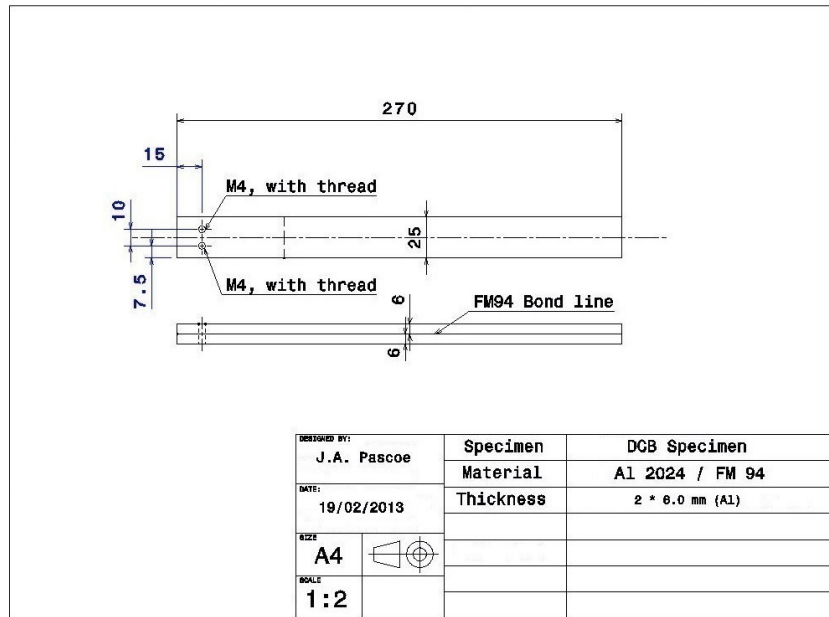


**Figure 3.1:** Dimensions of DCB specimens (Courtesy by John-Alan Pascoe, TU Delft)

equal to 125 mm, a width between 20 mm and 25 mm and an initial crack length of 50 mm measured from the line of load application. In this regard, loads are introduced into the specimen by loading blocks screwed to two threaded holes which were drilled after the curing. The application of load can therefore be considered to occur almost punctually in correspondence of the holes and they are used as a reference. See Figure 3.1 for the nominal dimensions.

The effective dimensions of each specimen have been accurately measured before testing, as will be described later.

Since the objective of the tests is researching the influence of adhesive layer thickness on crack propagation, specimens with different epoxy layers have been used. In particular two batches have been produced, denoted as *Type II* and *Type III*.

Type II batch was manufactured bonding the aluminium plates with two plies of resin, thus creating a double thickness of the adhesive with respect to that of the specimens tested in [4]. Each pre-preg ply consists of a nylon carrier soaked with epoxy resin; therefore the use of two plies involves the presence of two carriers. Specimens belonging to Type II have been denoted by letter *G*.

Type III batch was manufactured employing one single adhesive film with



**Figure 3.2:** Measurement station with Zeiss Axiovert 40 MAT

additional strips of FM94 U.06 resin film (without carrier). This arrangement should result in an intermediate thickness of the adhesive between the classical single ply and the double ply. Type III specimens have been denoted by letter *H*.

Two basic assumptions are implied behind the use of these specimens for testing. First of all it is virtually assumed that no contribution to the behaviour of the adhesive layer comes from the nylon matrix and that it does not influence crack propagation. This assumption is not actually grounded on a physical base since the inner matrix plays a role in the pattern of the adhesive; the influence of the carrier could be a topic for further studies. In the present work the adhesive layer is practically dealt with as homogeneous. The other main assumption is the constancy of thickness along the length of the specimen. The validity of this hypothesis will be discussed in more detail in the following.

Before starting tests the specimens have been measured to assess their exact dimensions. First of all the thickness of the adhesive layer has been measured by means of a *Zeiss Axiovert 40 MAT* inverted optical microscope (Figure 3.2); in this configuration the objective lenses and the light source are located below the stage pointing upward, while the object to be measured is placed on the stage itself, which is movable in its plane. This instrument can operate either in visual mode, manually focused by the user to visualize the object through a lens or, once set, acquiring pictures by a camera. In both modes the focus and the illumination, provided by a 100 W power supply,

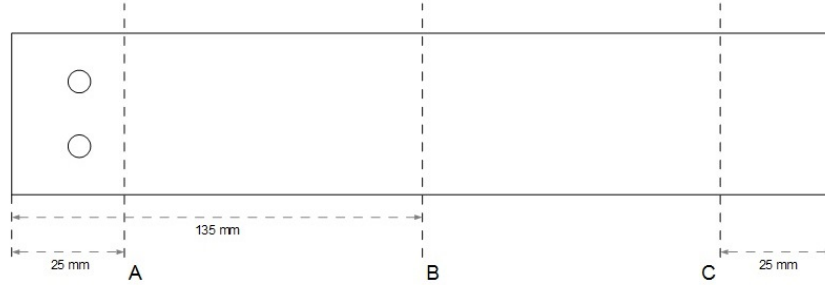


**Figure 3.3:** Location of measured points A, B, C

are regulated by a knob. Different objectives can be employed with varying magnification factors; a factor of 10 was used during the measurements. The acquired images have been elaborated by means of the software *AxioVision 4.8* to measure the thickness of the adhesive layer.

As prescribed by [1], pictures have been taken at different stations of the specimen, namely at 25 mm from both ends and at the midpoint. These locations have been denoted as A, B and C starting from the tip where the load is applied (Figure 3.3).

An example of the acquired pictures is shown in Figure 3.4, which has been captured at position A in specimen G-001. The interface between aluminium and adhesive film can be seen clearly and, from a deeper insight, the structure of the adhesive itself can be observed; the inner carrier is visible into the epoxy ply, represented by the dark spots which are the cross sections of the fibers composing it. The scale and the measurement taken using the elaboration software are also shown.

From a microscopic point of view the roughness of the aluminium surfaces produces many irregularities in the local thickness, that lead to the definition of an average value. In particular, the average thickness at each station has been defined as the mean between the minimum and the maximum values of the local thickness as measured from the pictures. Not only varies the thickness due to microscopic irregularities, but also remarkable variations have been found at different stations. Generally, locations A e B exhibit more roughness and a larger thickness, while location C is smoother and with a thinner layer.

These considerations pose a serious question whether the assumption of constant thickness is acceptable or not. What has been observed in the totality of the specimens is that the thickness decreases towards station C

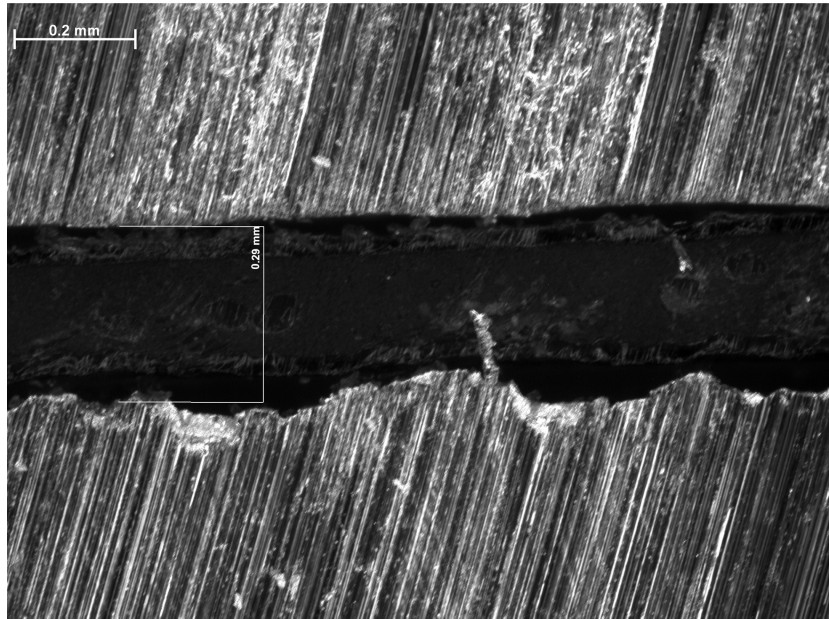


**Figure 3.4:** Microscopic picture of aluminium-epoxy interface

(in some cases even to one half of the value at the other tip), a fact probably due to epoxy bleeding during the manufacture process. On the other hand smaller variations have been measured between locations A and B.

The observation above has led to the choice of performing the tests on crack propagation in a region reasonably far from the tip, where the thickness is roughly constant. This is not a significant limitation, because the length of the specimens is enough to allow for proper measurements.

Beside measurements of the adhesive, the specimens were also measured by using a caliper to determine the exact values of length, width and thickness. Further details about the specimens, with tables and pictures, are provided in [Appendix A](#).

Eight out of twenty original specimens have been selected for fatigue tests. These account for four Type II and four Type III specimens to be tested at four different values of the R-ratio. The selection criterion is also explained in the appendix. Since the crack growth has been monitored visually by means of a camera, the chosen specimens have been set up in order to enhance the visibility of the crack. That basically consists in painting one side of the specimen with typewriter correction fluid (prepared samples are shown in [Figure 3.5](#)) so to obtain a white coating. This simple device creates contrast between the undamaged surface and the fracture path and is quite effective



**Figure 3.5:** Specimens coated with typewriter correction fluid

in showing up the crack.

A scale with reference points at intervals equal to 10 mm has been then marked on this coating to indicate the initial length of the crack and to easily check its propagation. A strip of graph paper has been stuck as well to allow for visual measurement of the crack length during the tests.

## 3.2 Experimental set-up and calibration

In order to research the influence of the adhesive thickness on crack propagation under cyclic loading, different specimens from the two batches have been tested. All tests have been led employing an *MTS 10 kN Elastomer* fatigue machine. This machine is powered by a hydraulic system and is controlled by the user through a computer. The user/machine interface reported in Figure 3.6 allows the user to set the machine parameters and to check the measurements while the test is running. On the right side of the picture a load-displacement calibration curve can be noticed, that will be discussed later.

The machine can measure or control a lot of different quantities, such as displacements, forces and strains and this gives the opportunity to run tests

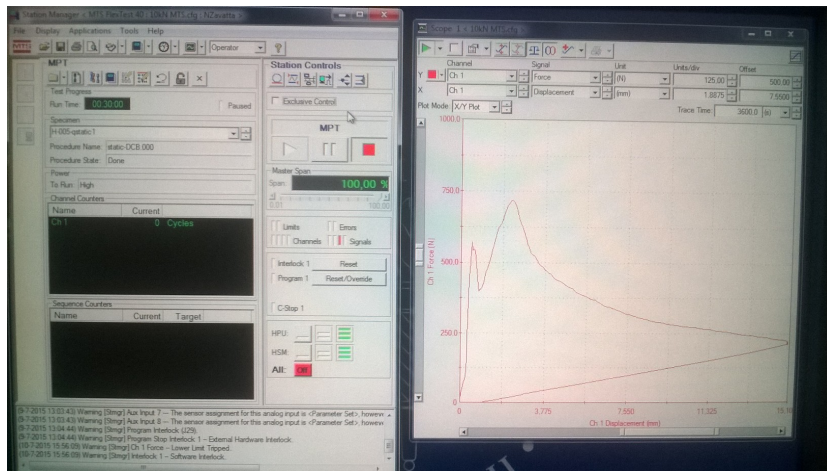


**Figure 3.6:** User/machine interface

either under displacement control or under force control. It is possible for the machine to apply both quasi-static and fatigue loads and the user can define the desired loading profile through the interface. Beside the options offered by the computer, a remote control is also provided that is handy for small adjustments, especially while the specimen is being mounted on the machine and during calibration. Two supports screwed to the machine have been fastened to the loading blocks attached to the specimens to provide the mounting. Attention must be paid to the integrity of the mounting to avoid that loose joints could lead to a detachment and to the failure of the test. A detailed picture of the mounting is given in Figure 3.7.

The technique used to measure the crack growth is an optical one and it is based on acquisition of pictures by a camera. The camera allows to check the crack growth while the experiment is running; however, the measurement of the crack length is not real-time and requires a post-processing activity. A key point for the effectiveness of this measurement technique is that the pictures must be clean and capture the crack under the best visibility conditions. This happens when no external motion is applied to the specimen and when crack opening is at its maximum. In order to fulfil these requirements, the acquisition of the pictures must be synchronized with the fatigue machine and a proper loading profile has to be used. The illumination needed to achieve adequate brightness in the pictures has been provided by a lamp. The complete experimental set-up is shown in Figure 3.8.

A key phase in testing is calibration. It is required both to properly set the instrumentation and to gather data needed in the subsequent tests. In order to provide clean pictures it is fundamental to have proper illumination

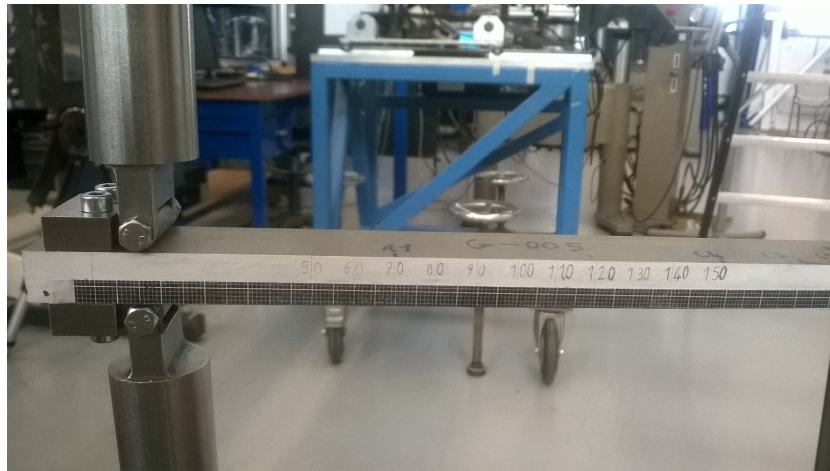


**Figure 3.7:** Mounting of the specimen on the machine

and to focus the images. This has been tuned manually checking the quality of the images on the display connected to the camera. The brightness can be set through the aperture of the lens, while manual zooming provides the focusing. Since the crack appears in the pictures as a dark line, its visibility is enhanced by slightly overexposing the pictures.

As far as concerns the specimens, a main point has to be explained. Although the specimens should theoretically be identical, it has already been pointed out that they slightly differ one another. These differences are responsible for small variations in their physical characteristics. This fact is taken into account by performing proper calibration prior to each test. Similarly to the tests, calibration has been displacement controlled and the applied force has been obtained as a measurement from the fatigue machine. A quasi-static loading profile has been used; it has been achieved through a ramp with a slope equal to 1 mm/min. For each specimen a load-displacement calibration curve has been plotted, like the one in Figure 3.9.

From this curve we can see that at the beginning the load increases rapidly with the displacement, because of the elastic force generated by the specimen, then it drops as the fracture of the adhesive bond starts. The load increases again during the (stable) fracture propagation phase, until it reaches a global maximum; after this point the crack growth becomes unstable and the load decreases. After having passed the critical point, the applied displacement is decreased until the force is zero; the non-zero value of the displacement at which this occurs is put as an offset. Typical values of the offset are around 0.3 mm. The value of the maximum load is a key result from calibration. In general choosing the values of the displacement applied in fatigue tests



**Figure 3.8:** Experimental set-up

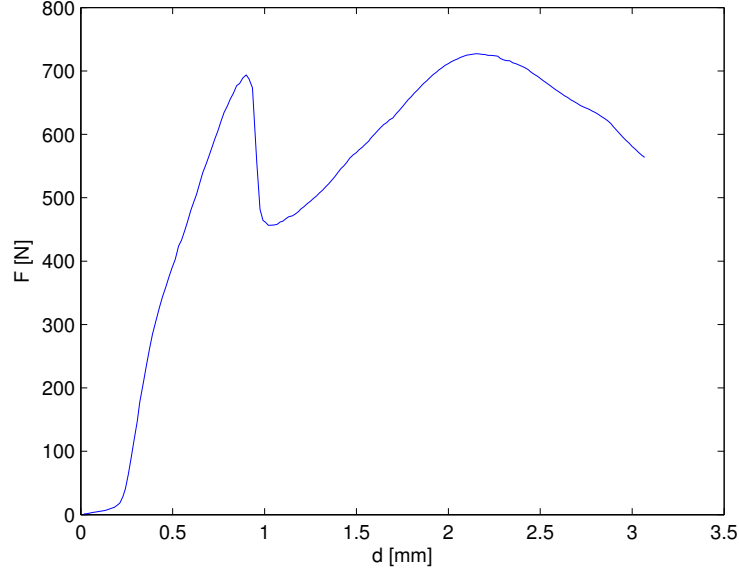


**Figure 3.9:** Load-displacement calibration curve of specimen G-010

is not easy. Since the main goal of testing is to investigate the effects of plasticity, the applied displacement has to be high enough to plasticize the material. Unfortunately, the stress distribution inside the specimen can be computed only through complex numerical simulations. For this reason a rough criterion has been used to determine the maximum displacement to be applied for fatigue testing: its value has been computed as a fraction of the displacement  $d_{F_{max}}$  at which the maximum force  $F_{max}$  was measured during quasi-static calibration. Called  $\delta$  this fraction, the maximum applied displacement is given by  $d_{max} = \delta d_{F_{max}}$ . The data gathered during calibration are summarized in Table 3.1<sup>1</sup>.

The reason for using different values of  $\delta$ , in particular larger values have been employed for specimens G-010 and H-008, is due to the fact that the crack grows very slowly at high R-ratios and a large displacement is preferable to obtain an appreciable growth.

---

<sup>1</sup>The first test with specimen G-006 encountered problems, thus calibration was repeated and a second test was run.

	$\delta$	$d_{F_{max}}$ [mm]	$F_{max}$ [N]
G-002	0.75	2.02	738.62
G-006*	1.25	2.16	725.75
G-006**	0.85	8.96	272.79
G-008	0.85	2.21	729.06
G-010	1	2.15	727.21
H-002	0.85	2.18	766.24
H-003	0.85	2.44	733.52
H-006	0.85	2.11	747.15
H-008	1	2.31	724.62

**Table 3.1:** Calibration results of the specimens used for fatigue testing

### 3.3 Fatigue testing

Fatigue tests have been run under displacement control, the force being measured by the machine. This choice has been suggested by the convenience of being consistent with [4] and by the technique used to monitor the crack growth. Controlling the displacement allows to synchronize the acquisition by the camera with the maximum applied displacement, i.e. the maximum crack opening. In order to do so a proper loading profile has to be used, like the one in Figure 3.10. This profile describes a single block and the loading that the specimen undergoes throughout the entire test is composed by its periodic repetition. We highlight here that, since the tests have been run under displacement control, the shown sequence actually refers to the applied displacement rather than to the load.

Station 1 represents the starting point, which is a zero displacement condition. It is important to notice that this does not generally imply zero force; conversely, if plasticity occurs into the specimen, a significant amount of force may be required to have zero displacement. From point 1 the displacement is increased through a ramp up to point 2. The displacement is at a maximum, as well as the crack opening and the specimen is still. This condition is held for 7 seconds, during which a picture is taken. Then fatigue loading starts and the displacement is cyclically decreased and increased between level 2 and level 3. The number of fatigue cycles varies throughout each test. At the beginning the crack growth is faster and a larger amount of pictures is required for proper monitoring; after this initial phase the crack growth slows down and the number of fatigue cycles can be increased. In the tests a number of cycles equal to 102 and 1002 has been respectively used. The frequency has been set equal to 5 Hz. After cyclic loading the specimen is

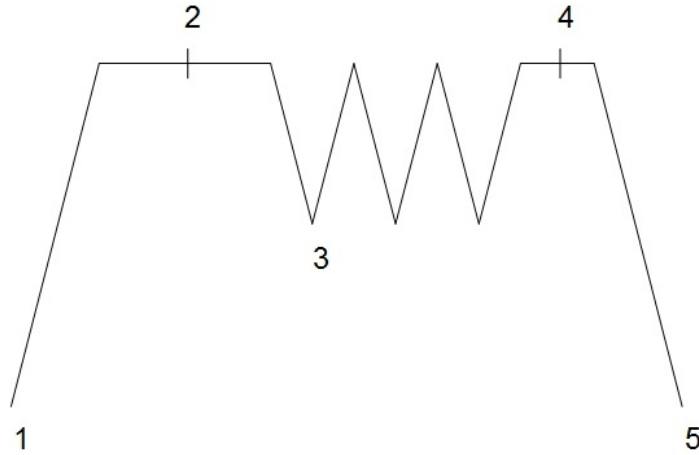


**Figure 3.10:** Profile of the applied displacement

held at level 4 for 5 seconds, then the displacement decreases to the initial value (point 5).

As the tests are displacement controlled, it is convenient to define a ratio between maximum and minimum displacements in a similar way to the R-ratio defined using the loads. This ratio is called  $R_d$  and is computed simply as  $R_d = \frac{d_{min}}{d_{max}}$ . Recalling the expression of the R-ratio  $R = \frac{P_{min}}{P_{max}}$ , we can notice that these two ratios are strictly related each others. In case of linear elastic materials, loads and displacements are proportional and it can be easily proved that  $R_d = R$ . If plasticity occurs, the linear relation between load and displacement is no longer valid; in this case  $R_d$  and  $R$  can be related through a nonlinear curve given by experimental data. In the following we will freely to both these ratios as R-ratio.

Four different values of  $R_d$  have been employed for testing. Each specimen has been tested at one single  $R_d$  in such a way that each of the two batches is tested at every value of  $R_d$ . The applied displacement has been computed as explained in the previous section. The ratio  $R_d$ , the maximum applied displacement  $d_{max}$ , the maximum load  $P_{max}$  measured by the machine and the number of cycles  $N$  are reported in Table 3.2.

The first specimen to be tested was G-006; during the test a problem occurred that stopped the machine. As a result a second test was run with the same specimen at the same  $R_d$ . Prior to start the test a new calibration has been performed to take into account the modification of the physical

	$R_d$	$d_{max}$ [mm]	$P_{max}$ [N]	$N$ [cycles]
G-002	0.29	1.52	362.69	356100
G-006*	0.036	2.69	413.42	23000
G-006**	0.036	7.57	113.02	305100
G-008	0.61	1.88	324.86	345300
G-010	0.86	2.15	396.86	298600
H-002	0.036	1.85	319.18	345100
H-003	0.29	2.07	366.45	342000
H-006	0.61	1.79	346.47	363100
H-008	0.86	2.31	496.23	350100

**Table 3.2:** Data concerning fatigue testing

properties of the specimen due to the fatigue cycles undergone during the first test. As expected, a decrease of the elastic modulus has been observed as a consequence of crack growth. Data relating to the two tests are denoted respectively by G-006\* and G-006\*\*.

All the tests have been stopped before complete fracture of the specimen. Typically the crack has reached a length of about  $70 \div 80$  mm, which is more or less one half of the total length of the strip of graph paper used to measure it. Due to the availability of the machine the number of cycles per test is slightly variable, with values around  $300 \div 350$  kcycles.

The machine acquires data at the beginning of the fatigue segment of each block, with a sampling frequency equal to 10 Hz. The data acquired by the machine and the pictures taken by the camera have been stored in order to be processed. The pictures have been post-processed by means of a program for the elaboration of images and the crack length has been measured by a visual comparison with the graph paper attached to the specimen. This method is consistent with the one employed in [4]. The limitations of this measurement technique concern the difficulty to achieve a good accuracy when slow crack growth is involved, as illustrated in section 4.2.

### 3.4 Quasi-static testing

In addition to fatigue testing, two tests have been conducted under quasi-static conditions to assess the influence of the adhesive thickness on crack growth in absence of fatigue. The specimens selected for quasi-static tests belong to the two original batches; in particular G-005 and H-005 have been used.

Similarly to fatigue tests, also quasi-static ones have been run under displacement control. In this case the tests have not been preceded by a calibration procedure. The applied displacement follows a ramp profile, with a slope equal to 0.5 mm. Tests have been stopped as soon as the displacement reached a value  $d = 15$  mm. As expected, a significant amount of plasticity is induced into the specimens and the residual displacements  $d_{res}$  left into the specimens after they are unloaded are respectively  $d_{res} = 1.36$  mm for G-005 and  $d_{res} = 0.94$  mm for H-005.

Data have been acquired by the machine at a sampling frequency of 2 Hz. This results in a sampling time equal to 0.5 s. Since the tests are quasi-static, the crack is continuously held at its maximum opening; moreover, no abrupt movement is applied to the specimen. For these reasons the pictures taken by the camera are clear and capture well the crack. As a consequence no problem has been encountered during the processing of the images. *Excel* and *MATLAB* codes have been used to elaborate the acquired data. The results of quasi-static testing are shown in the following chapter.

# Chapter 4

## Experimental results

In chapter 3 the experimental set-up and the procedures used to run the tests have been described. The data acquired by the machine have been processed by means of *Excel* to put them in a more organised form. Then a *MATLAB* program has been developed to compute the quantities required for data analysis and to plot the graphs shown in the following. We will first deal with the computation of crack length and of energy. As far as concerns fatigue testing, we will show the correlation between crack growth rate and strain energy release rate and between crack growth rate and cyclic strain energy. Results concerning quasi-static tests are also shown.

### 4.1 Crack length measurement in fatigue tests

The crack length has been measured from the pictures. The number of pictures considered for the measurement has been generally less than the number of acquired pictures. In effect it is not possible to visually detect very small increments in the crack length. Considering every acquired picture only leads to a huge amount of work and time needed for analysis without any real gain; thus only a limited number of pictures gives a valuable contribution to the determination of crack growth. More pictures have been used to capture the propagation of the crack during the initial phase, when the growth is faster, while the number decreased past this phase. Usually 1/5 of the pictures has been considered in the initial phase and 1 out of 10 ÷ 20 pictures towards the end of the test. Another factor that strongly influences the crack measurement is the R-ratio. The tests run at the highest R-ratio have exhibited very slow crack growth. Measuring this slow growth is not an easy task; we will return to this point at the end of this section.

The measurements of the crack taken from the pictures have not been

	$k$	$m$	$c$	$RMSE$
G-002	42.79	0.03788	0	1.044
G-006*	43.94	0.04225	12.51	0.8011
G-006**	0.2818	0.3663	138.2	0.6598
G-008	0.009334	0.5101	58.73	0.2956
G-010	61.01	0.0003143	0	0.03131
H-002	43.79	0.04914	0	1.336
H-003	1.72	0.2145	57.72	0.7801
H-006	0.00911	0.5406	58.42	0.4553
H-008	0.004994	0.5283	60.9	0.1894

**Table 4.1:** Values of the coefficients in equation (4.1) and  $RMSE$

used directly in the analysis. Instead, a regression of the measured data has been performed to obtain a continuous curve. The values provided by this curve have been employed to relate the crack growth to the data acquired by the machine. The *MATLAB* toolbox *Curve Fitting Tool* has been used to perform the regression. Denoting the crack length with  $a$  and the number of cycles with  $N$ , a continuous function  $a = a(N)$  has been obtained. Good results can be achieved employing a power function in the form:

$$a(N) = kN^m + c. \quad (4.1)$$

The empirical coefficients  $k$ ,  $m$  and  $c$  are computed by the curve fitting algorithm according to a nonlinear least square method and the goodness of fit is evaluated in terms of Root Mean Square Error ( $RMSE$ ); the lower the  $RMSE$ , the closer the fit is to the data. In Table 4.1 are shown the values of the coefficients and the error for each test.

The fitting curve does not correctly represent the crack length when  $N$  tends to 0. In addition to that, the initial crack length differs slightly from one test to another, because it is dependent on the maximum displacement applied during calibration. However, the main purpose of the fitting is to evaluate the increase of the crack length rather than its absolute value. This can be done considering the slope of the curve; to this extent no contribution comes from the initial crack length, i.e. the coefficient  $c$ . Indeed the curve fits well the data trend for  $N > 0$  and the slope is preserved. The curves obtained for each test are plotted in Figure 4.1 on a semi-logarithmic scale. Concerning specimen G-006, only data regarding G-006\*\* are shown, because the first test G-006\* provided a small amount of measurements.

The crack growth rate can be computed by taking the derivative of (4.1)

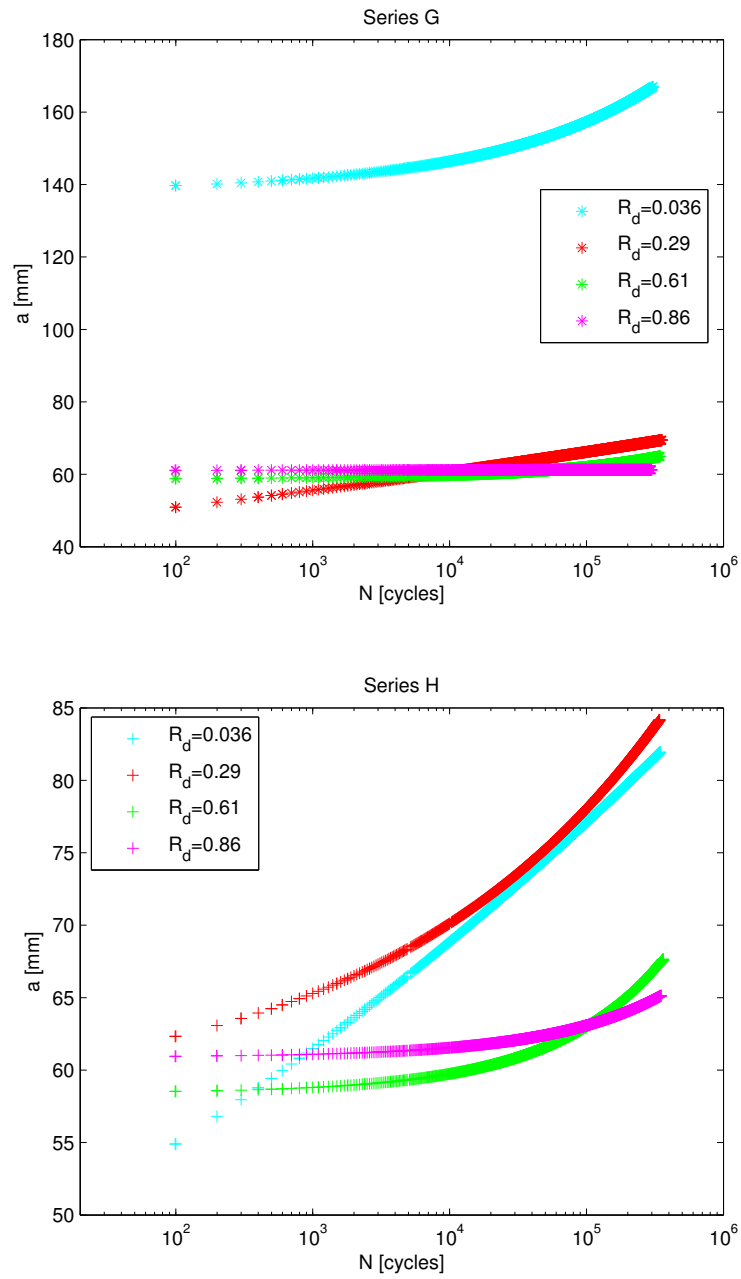


**Figure 4.1:** Plot of the crack length against the number of cycles

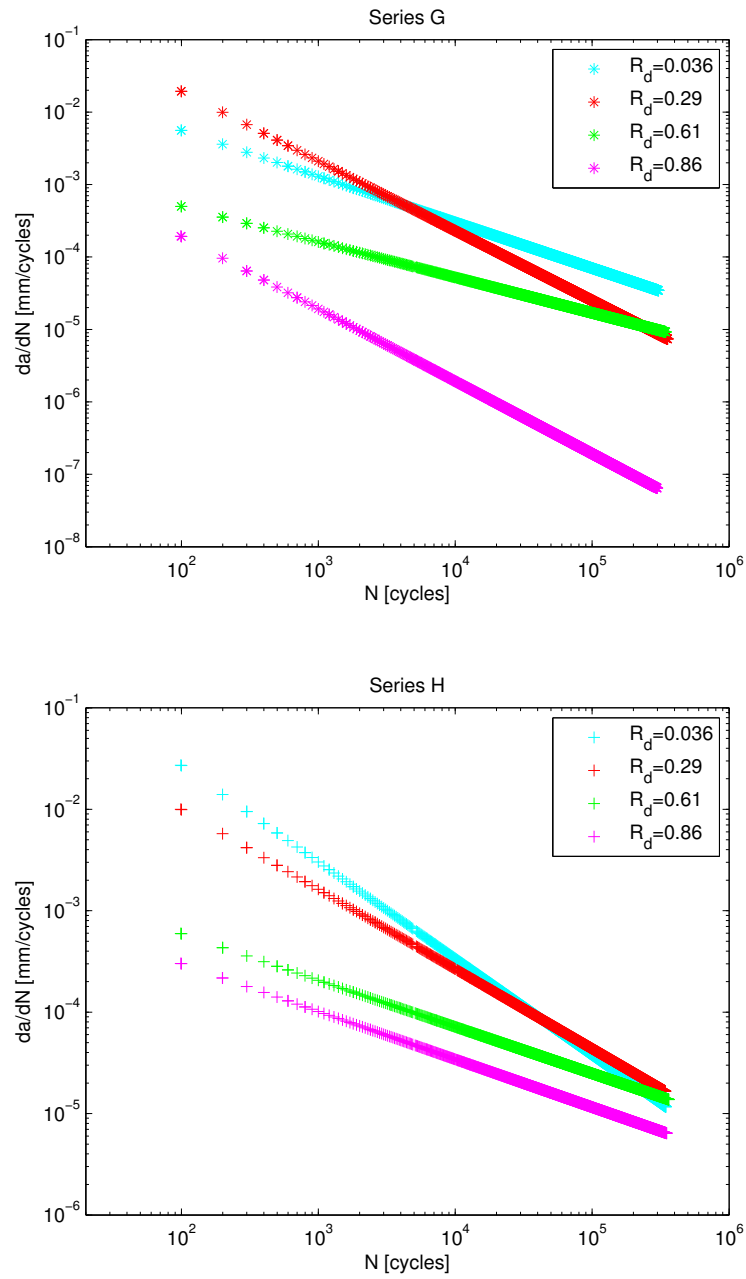


Figure 4.2: Crack growth rate against the number of cycles

	$k$	$m$	$c$	$RMSE$
G-005	6.436	0.4282	-18.76	0.4394
H-005	6.551	0.4271	-20.03	0.6918

**Table 4.2:** Coefficients in equation (4.3) and  $RMSE$ 

with respect to  $N$ . This yields the following expression:

$$\frac{da}{dN} = mkN^{m-1}. \quad (4.2)$$

The quantity  $\frac{da}{dN}$  is the instantaneous crack growth rate and can be seen as the increase of crack length per unitary cycle. According to theory, it plays a central role in the analysis of the crack growth phenomenon. In Figure 4.2 the outcomes from equation(4.2) are shown on a logarithmic plot. As expected, the crack growth is initially very fast. Subsequently it slows down and, at limit, the growth rate tends asymptotically to 0, as a consequence of  $m < 1$  in (4.2). In general we can notice that the crack growth rate is higher for low values of  $R_d$ . This fact is not surprising since, at  $d_{max}$  almost constant, a low  $R_d$  results in a larger loading amplitude.

The tests led with the highest R-ratio, namely  $R_d = 0.86$  for specimens G-010 and H-008, exhibited a very little crack growth, to such an extent that the measured values of the crack length ought to be considered very carefully. To the scope of the present research, no conclusion should be drawn, that is based only on results from the aforementioned tests.

## 4.2 Crack length measurement in quasi-static tests

As in the case of fatigue tests, the measurement of the crack length has been performed through the acquired pictures. In both specimens G-005 and H-005 the first picture was taken at  $t = 260$  s, that is the point about which crack propagation becomes unstable. The crack growth has been analysed as a function of time. A curve in the same form as (4.1) has been employed to fit the data, namely:

$$a(t) = kt^m + c. \quad (4.3)$$

The coefficients  $k$ ,  $m$  and  $c$  are shown in Table 4.2. The limitations concerning the fitting curve already expressed in case of fatigue tests still

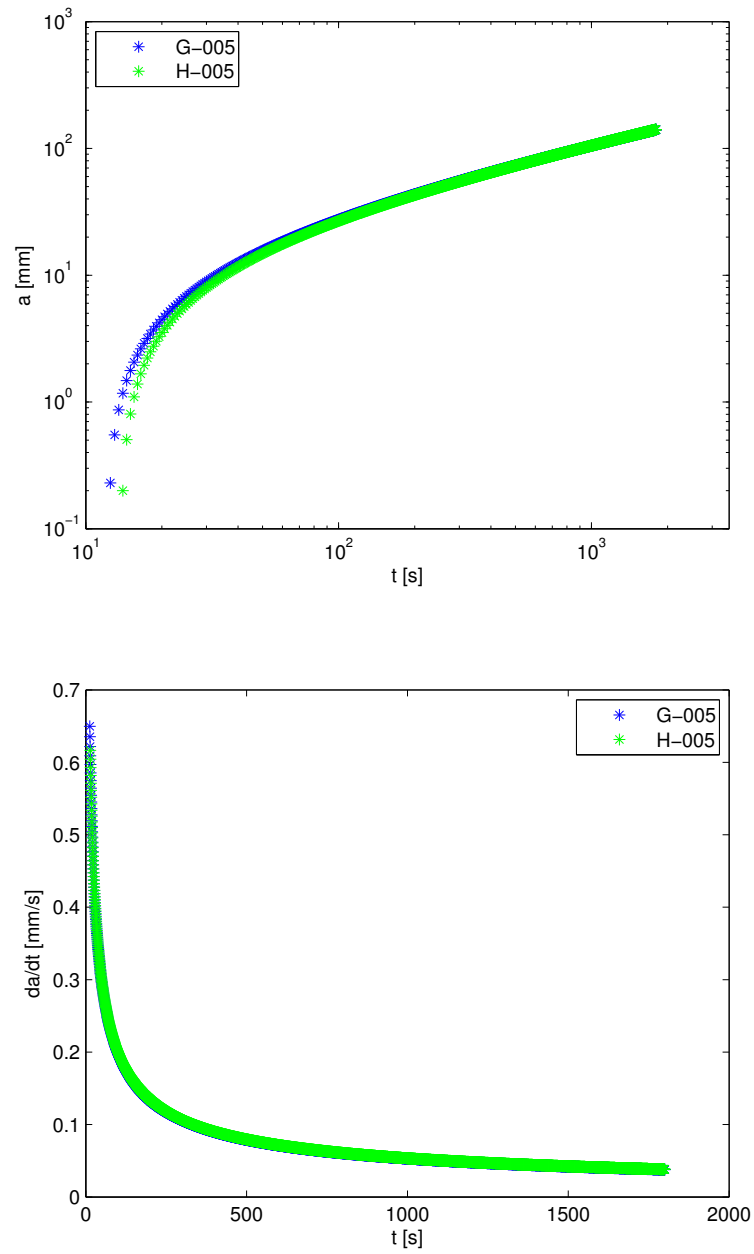


**Figure 4.3:** Crack length and crack growth rate in quasi-static conditions

hold true; extrapolation of the curves for  $t < 260$  s provides only rough results. The crack growth rate in quasi-static conditions has been computed by differentiating the previous equation, resulting in:

$$\frac{da}{dt} = mkt^{m-1}. \quad (4.4)$$

The outcomes from equations (4.3) and (4.4) are illustrated in Figure 4.3.

### 4.3 Energy calculation in fatigue testing

Besides the computation of crack length and crack growth rate, calculations concerning the energy have also been carried out. Computing the energy requires the knowledge of applied forces and displacements, that have been taken from the measurements acquired by the machine.

The measurements from the machine are such that for any loading block two samples are acquired. The first sample contains the value of the minimum applied displacement  $d_{min}$  and the force  $P_{min}$  measured at that displacement. The second sample is taken at the maximum applied displacement  $d_{max}$  and the corresponding value of the force  $P_{max}$  is measured. One set of measurements  $\{d_{min}, P_{min}, d_{max}, P_{max}\}$  is obtained for each block.

Two different types of energy have been computed, namely cyclic energy and total energy. The cyclic energy is denoted by  $U_{cyc}$  and represents the energy stored into the specimen in a single loading cycle. Given a set of measurements, the cyclic energy can be computed in an approximate way according to the formula:

$$U_{cyc} = \frac{1}{2}(P_{min} + P_{max})(d_{max} - d_{min}).$$

The total energy is denoted by  $U_{tot}$  and is the sum of the cyclic energy and of the monotonic energy at one single cycle. Similarly to  $U_{cyc}$ , an approximate expression can be used to compute the total energy:

$$U_{tot} = \frac{1}{2}P_{max}d_{max}.$$

Though exact only if the load-displacement relationship were fully linear, the above expressions have been used to estimate the energy given to the specimens during loading. The results for the two batches of specimens are shown in Figures 4.4 and 4.5.

The data show a monotonic decrease of both the cyclic energy and of the total energy with the number of cycles. This trend is in line with what is predicted by the theory. Indeed, the energy stored into the specimen is

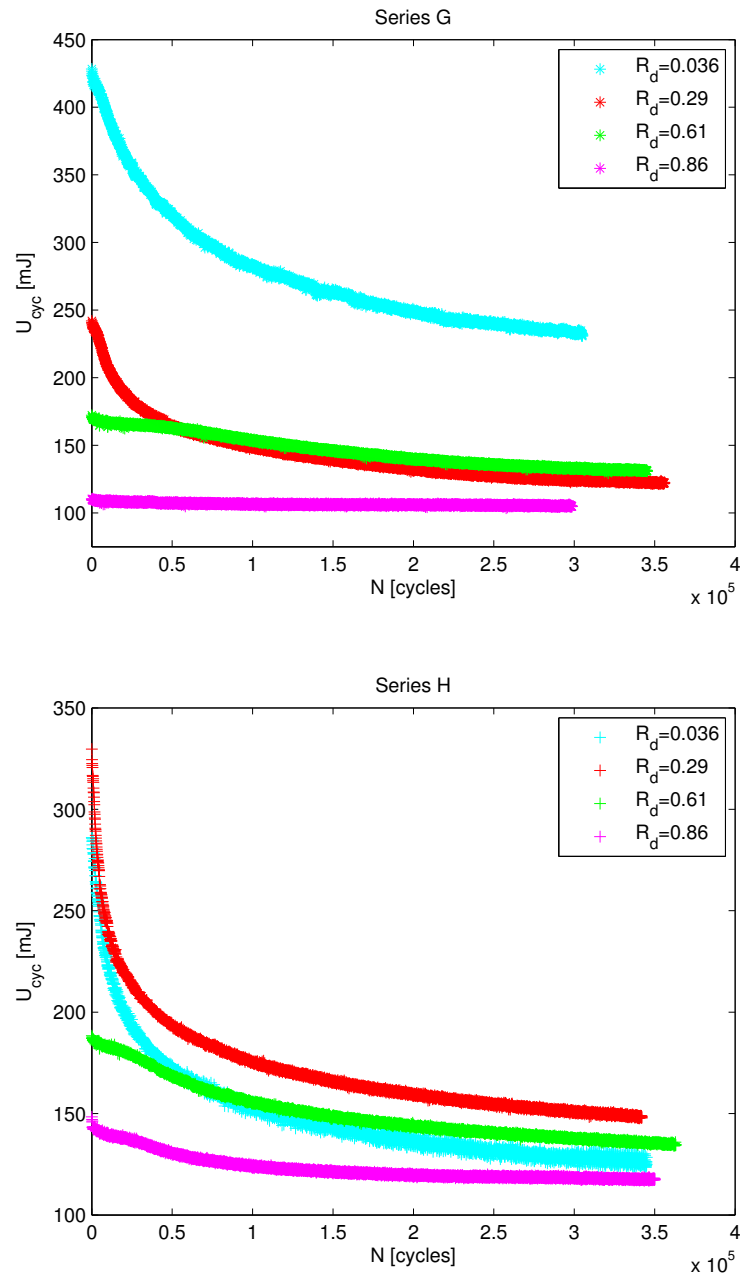


**Figure 4.4:** Cyclic energy trend from experimental data

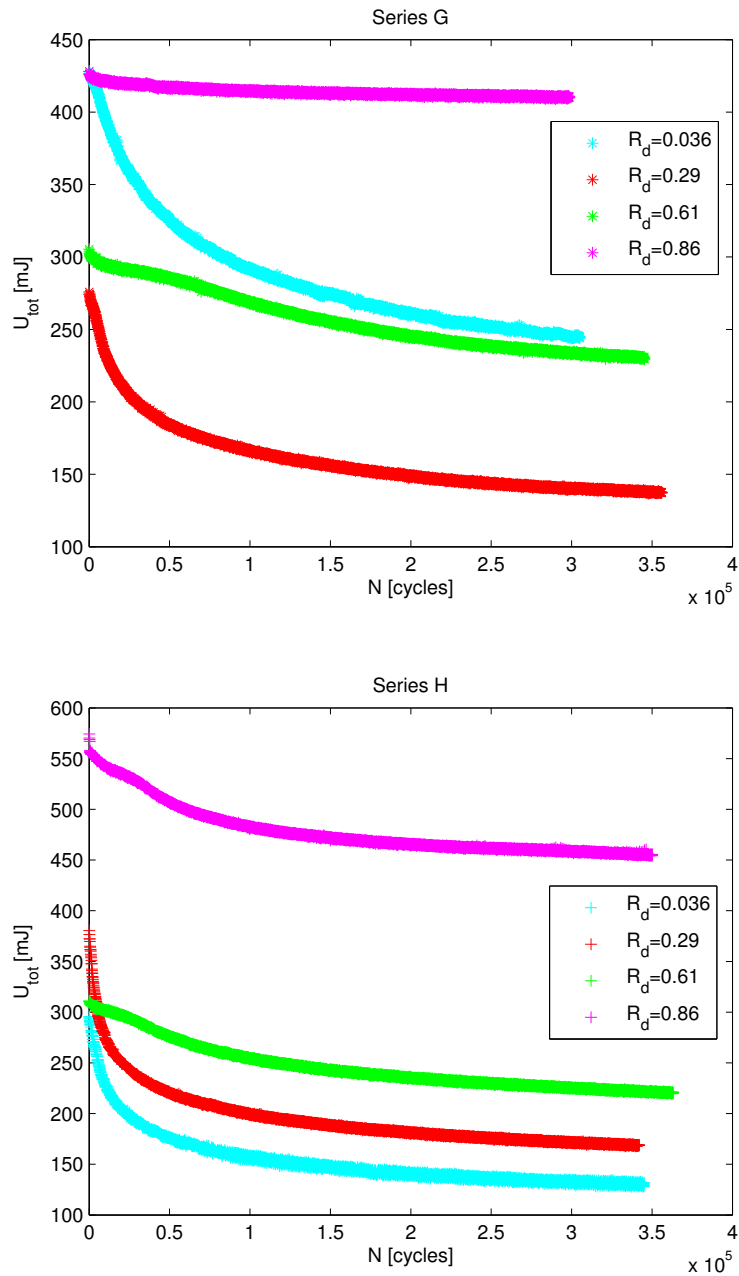


Figure 4.5: Total energy trend from experimental data

	$a_1$	$b_1$	$c_1$	$RMSE$
G-002	31670	-0.000445	-31420	3.120
G-006*	-137.4	0.1453	775.8	6.273
G-006**	-48.12	0.161	593.6	6.832
G-008	-0.018	0.6156	174.6	5.028
G-010	117.9	-0.008499	0	9.662
H-002	1345	-0.02629	-839.1	6.103
H-003	872.8	-0.05224	-301.8	6.348
H-006	-1.838	0.2915	209.6	3.939
H-008	-14.27	0.1193	182.1	12.19

**Table 4.3:** Coefficients in the fitting curve of  $U_{cyc}$

proportional to the elastic modulus  $E$ . During fatigue loading the amount of damage occurring into the specimen, i.e. the crack growth, causes the elastic modulus to decrease; since the tests are displacement controlled and the ratio  $R_d$  is fixed throughout the test, the energy decreases monotonically.

Generally, the higher  $R_d$ , the lower is the cyclic energy. This can be easily understood, because the value of  $d_{max}$  is approximately the same in each test and this implies a smaller difference  $d_{max} - d_{min}$  as  $R_d$  increases. Conversely, an increase of  $U_{tot}$  with  $R_d$  can be observed, due to the larger amount of monotonic energy given to the specimen and to a smaller decrease of the elastic modulus (the crack grows less, see section 4.1).

The computed values of  $U_{cyc}$  and  $U_{tot}$  have undergone a regression procedure similar to that explained for  $a$  to express them as a function of the number of cycles  $N$ . Suitable fitting curves have been found in the form of power functions, which are formally equal to (4.1).

As far as the cyclic energy is concerned, the following function has been employed:

$$U_{cyc}(N) = a_1 N^{b_1} + c_1 \quad (4.5)$$

where the coefficients  $a_1$ ,  $b_1$  and  $c_1$  have been computed by means of *Curve Fitting Tool* and are reported in Table 4.3 together with the root mean square error.

Not dissimilarly at all, the curve for the total energy is given by:

$$U_{tot}(N) = a_2 N^{b_2} + c_2 \quad (4.6)$$

and its coefficients are collected in Table 4.4.

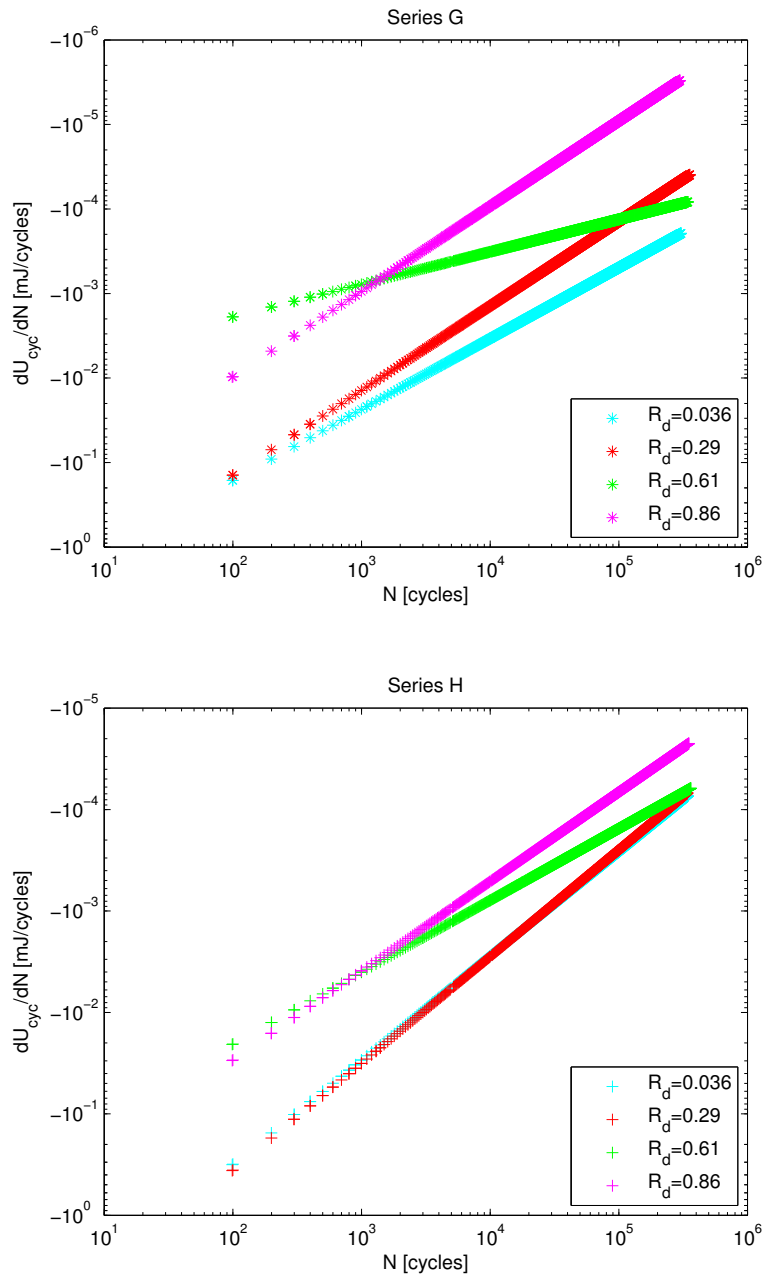


Figure 4.6: Logarithmic plot of  $\frac{dU_{cyc}}{dN}$  as a function of  $N$

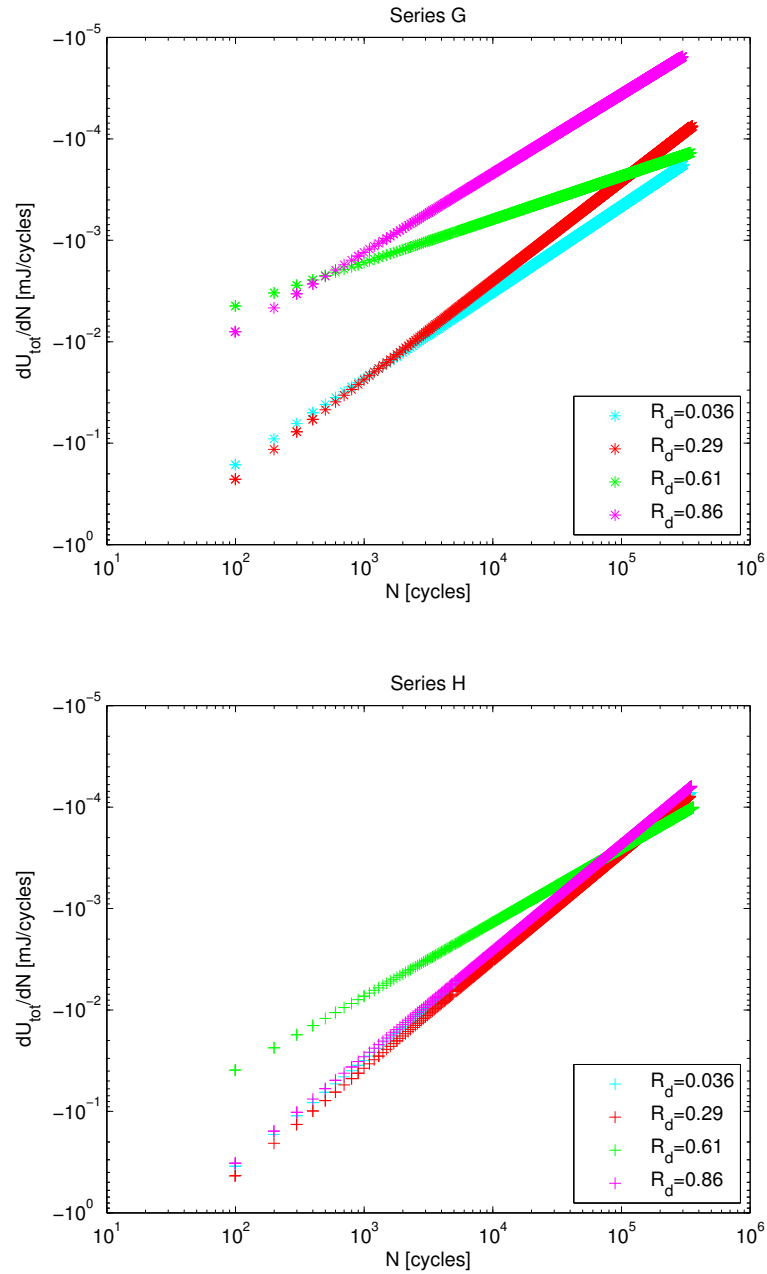


Figure 4.7: Logarithmic plot of  $\frac{dU_{tot}}{dN}$  as a function of  $N$

	$a_2$	$b_2$	$c_2$	$RMSE$
G-002	-1037	0.01993	1472	5.095
G-006*	-1169	0.03693	1926	4.235
G-006**	-54.04	0.1506	601.3	6.369
G-008	-0.05518	0.5733	308.4	6.538
G-010	-1.31	0.22	431.2	3.514
H-002	1014	-0.04127	-471.9	6.268
H-003	964.9	-0.05814	-293.3	7.250
H-006	-4.088	0.2724	350.7	5.740
H-008	839.3	-0.04787	0	7.197

**Table 4.4:** Coefficients in the fitting curve of  $U_{tot}$

Equations (4.5) and (4.6) have been differentiated with respect to  $N$ , yielding the following expressions:

$$\frac{dU_{cyc}}{dN} = a_1 b_1 N^{b_1-1}, \quad (4.7)$$

$$\frac{dU_{tot}}{dN} = a_2 b_2 N^{b_2-1}. \quad (4.8)$$

The quantities  $\frac{dU_{cyc}}{dN}$  and  $\frac{dU_{tot}}{dN}$  represent the instantaneous variation of the energy; from a physical point of view, they can be regarded respectively as the loss of cyclic and total energy stored into a specimen per cycle, due to the increase of the crack length. They are plotted in Figures 4.6 and 4.7 against the number of cycles.

## 4.4 Energy calculation in quasi-static testing

The load-displacement curves obtained in quasi-static tests are plotted in Figure 4.8. These curves are basically similar to the calibration curve shown in section 3.2. The first local maximum denotes the fracture initiation. From about  $t = 260$  s the load starts to decrease monotonically, indicating that unstable crack growth has taken place. We introduce the following notation: the quantities measured at the  $t$ -th time instant are denoted by the subscript  $t$ . The energy  $U_t$  is the total energy given to the specimen from the starting point  $t = 0$  to the  $t$ -th instant and is represented graphically by the area under the load-displacement curve comprised between 0 and  $d_t$ . It can be

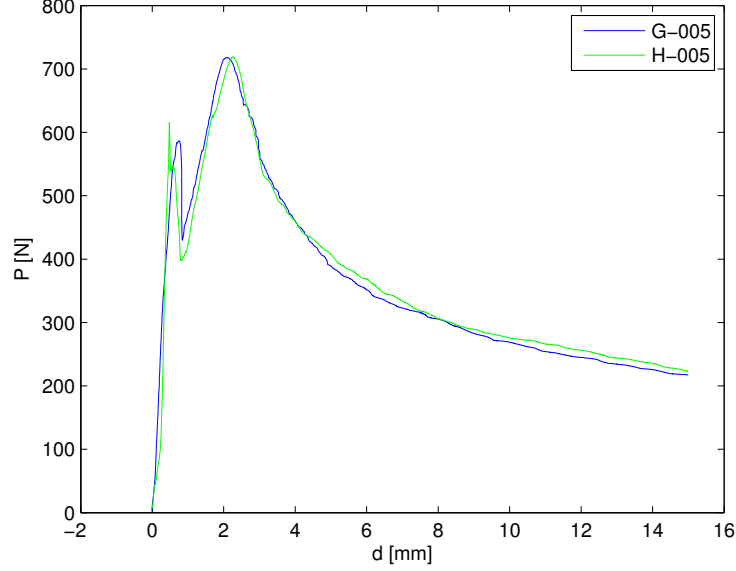


**Figure 4.8:** Load-displacement curve from experimental data

computed according to:

$$U_t = \frac{1}{2}(P_t + P_{t-1})(d_t - d_{t-1}) + U_{t-1}$$

$$U_1 = \frac{1}{2}P_1d_1$$

This expression implements the trapezoidal rule for the numerical calculation of integrals in a recursive form. A plot of  $U_t$  versus  $t$  is given in Figure 4.9. By definition of  $U_t$ , the curve is monotonically increasing. An inflection point can be noticed in the curve as crack growth becomes unstable at  $t = 260$  s, denoting that less and less energy is required due to the drop of stiffness. Following a procedure similar to that used in the fatigue case, the values of the energy have been fitted by a curve, whose equation is:

$$U(t) = at^b + c. \quad (4.9)$$

Coefficients  $a$ ,  $b$  and  $c$  are shown in Table 4.5. The fitting has been performed considering  $t \geq 260$  and values under this limit are unrealistic. Equation (4.9) has been derived with respect to  $t$  yielding:

$$\frac{dU}{dt} = abt^{b-1}. \quad (4.10)$$

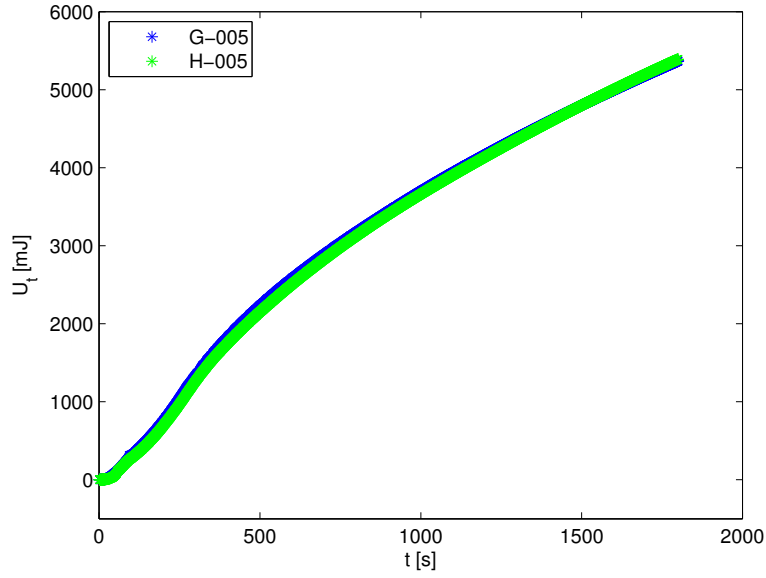


Figure 4.9: Plot of the energy  $U_t$  against time  $t$

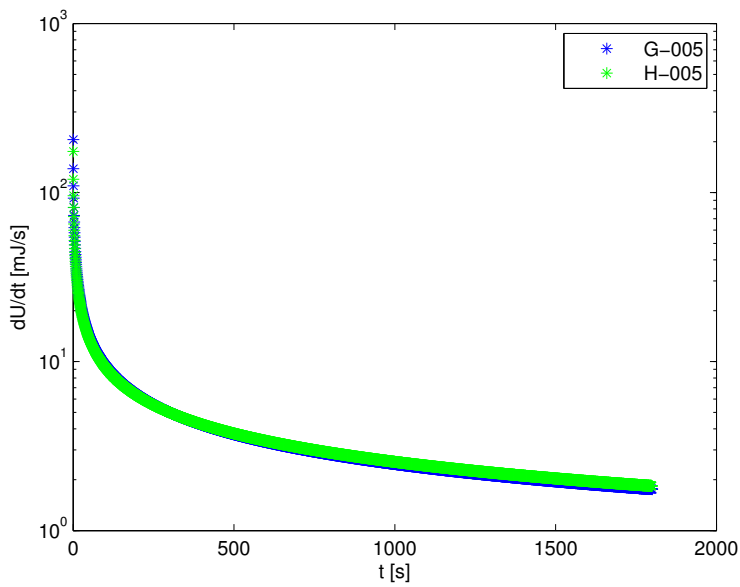


Figure 4.10: Semi-logarithmic plot of  $\frac{dU}{dt}$  versus  $t$

	$a$	$b$	$c$	$RMSE$
G-005	334.7	0.4166	-2242	10.1
H-005	273.1	0.4418	-2110	9.24

**Table 4.5:** Coefficients in equation (4.9)

The quantity  $\frac{dU}{dt}$  is the instantaneous energy release due to the increment of crack length. The outcomes from equation (4.10) are plotted in Figure 4.10.

## 4.5 Crack growth rate as a function of SERR

The strain energy release rate  $G$  can be computed according to the methods described in section 2.3. Since the difference between the three proposed methods is tiny, we have decided to employ the simple MBT (Modified Beam Theory) method. The SERR is computed through the following equation:

$$G = \frac{3Pd}{2aw}$$

where  $P$  is the measured load,  $d$  is the applied displacement,  $a$  is the crack length and  $w$  is the width of the specimen under examination. Following an usual approach, it is possible to explicit the dependence of the crack growth rate on the computed SERR. As discussed in chapter 2, different functions of  $G$  can be used to establish such a correlation: in this study  $G_{max}$  and  $\Delta\sqrt{G}$  have been employed. These two choices lead to the curves shown in Figure 4.11 and 4.12. Their trend is similar to that of the curves illustrated in [4]. The correlation curves show a net dependence on the R-ratio; in particular there is a separation between curves obtained at different ratios. This is true either when the curves are plotted against  $G_{max}$ , either when the plot is referred to  $\Delta\sqrt{G}$ . This dependence is in line with what has already been observed by other authors. As far as concerns the thickness of the adhesive, no appreciable difference can be observed between the two batches of specimens.

Comparing tests run at different R-ratios on basis of the strain energy release rate is somewhat questionable because of the reasons already discussed in section 2.1.

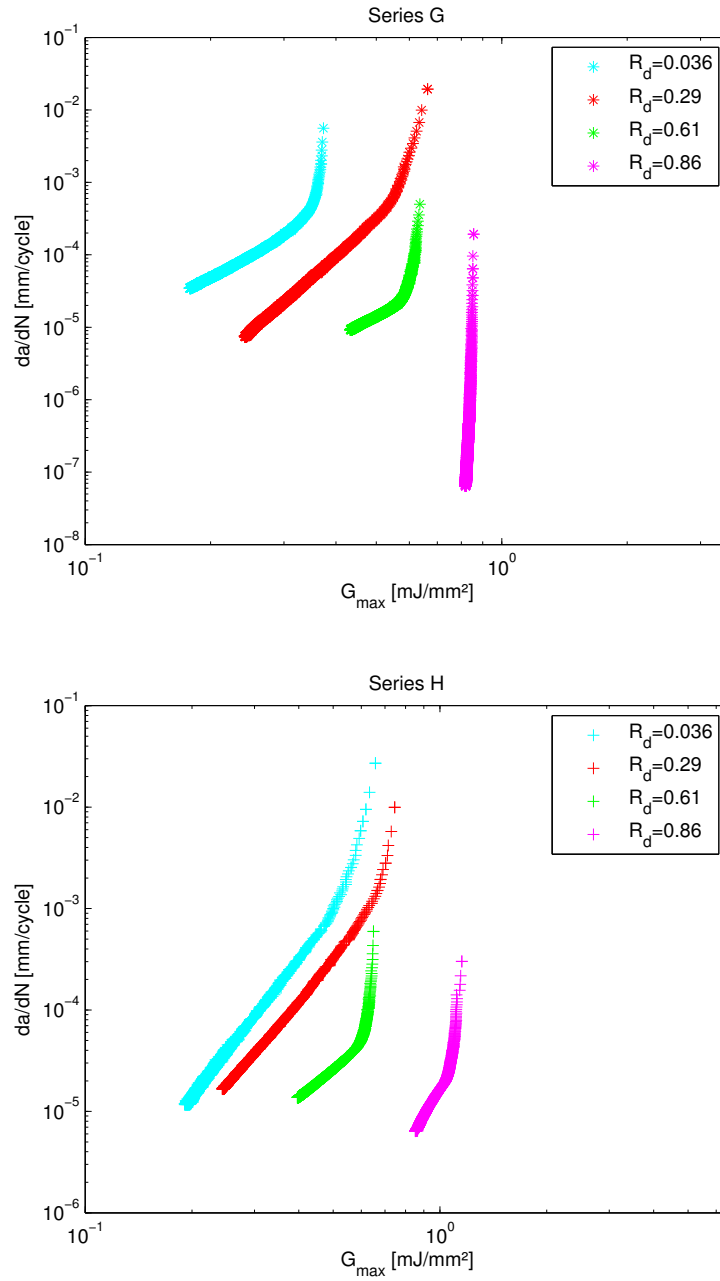


Figure 4.11: Logarithmic plot of  $\frac{da}{dN}$  against the maximum SERR

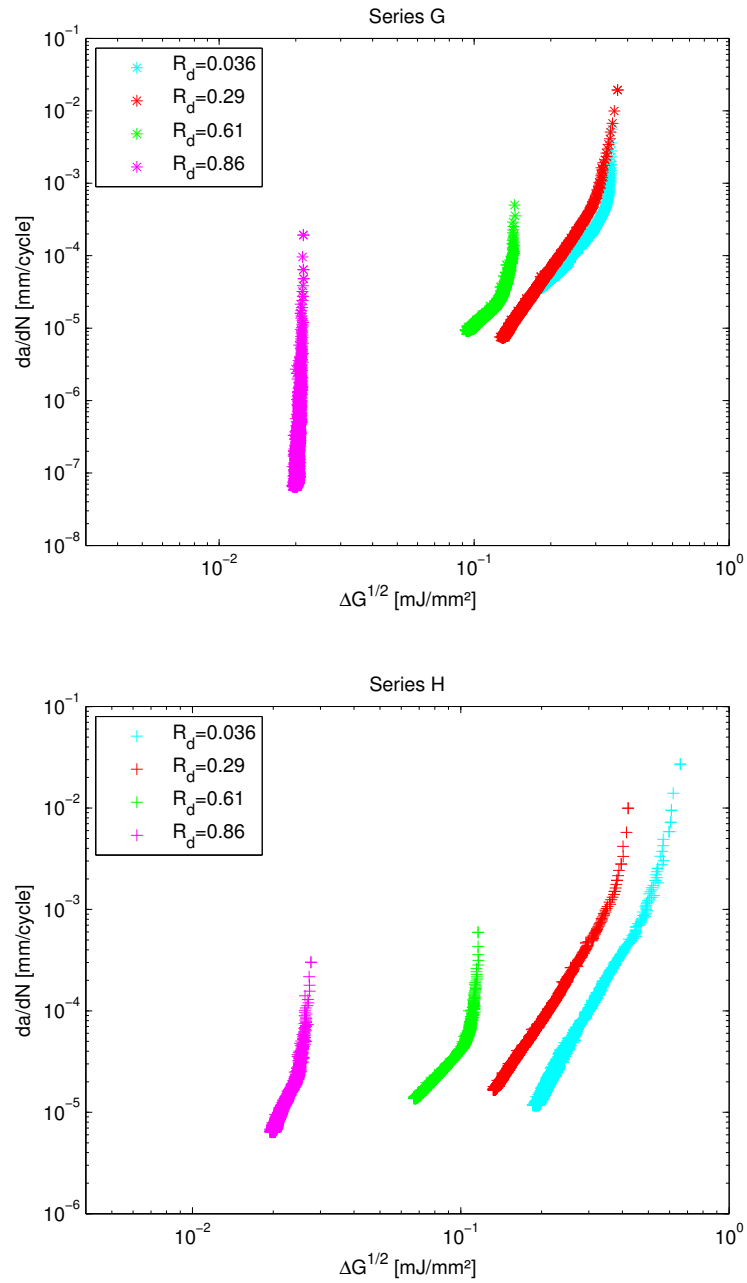


Figure 4.12: Logarithmic plot of the crack growth rate against  $\Delta\sqrt{G}$

## 4.6 Crack growth rate related to cyclic energy

Conversely to the approach illustrated in the previous section, the one described in the following aims at a complete characterisation of crack growth by means of a single parameter. The correlation between crack length and energy release is established on a *per cycle* basis, considering the derivatives  $\frac{da}{dN}$ . The quantities involved, namely  $\frac{dU_{cyc}}{dN}$  and  $\frac{dU_{tot}}{dN}$ , have already been discussed in section 4.3. The parameters usually employed to describe a cycle, like the R-ratio or the maximum amplitude, are all taken into account in the definition of the energy.

In Figure 4.13 and 4.14 the correlation between  $\frac{da}{dN}$  and  $\frac{dU_{cyc}}{dN}$  and between  $\frac{da}{dN}$  and  $\frac{dU_{tot}}{dN}$  is shown. Actually, the crack surface  $A$  is considered instead of the length  $a$ . We assume that the crack front is a straight line; under this hypothesis the crack surface can be computed by simply multiplying  $a$  by the width of the specimen under exam (provided in Appendix A). Simply, their derivatives result in  $\frac{dA}{dN} = w \frac{da}{dN}$ .

The results in the figures are consistent with the findings illustrated in [4]. According to section 2.2, a power-law can be fitted through the data, resulting in the following relationships:

$$\frac{dA}{dN} = C \left( \frac{dU_{cyc}}{dN} \right)^n \quad (4.11)$$

$$\frac{dA}{dN} = C \left( \frac{dU_{tot}}{dN} \right)^n \quad (4.12)$$

The coefficients  $C$  and  $n$  have been obtained by Pascoe et al. and their values are collected in Table 4.6 together with the coefficient of determination  $R^2$ . The authors also point out that the correlation is better when considering the release of cyclic energy instead of that of total energy (because  $R^2$  is closer to 1), but the reason for this is unknown. The power curve is represented as a blue straight line with slope  $n$  and intercept  $\log C$  on the logarithmic plots in the figures.

Similarly to what is done in [4], it is possible to compute the coefficients  $C$  and  $n$  according to our set of data and discriminating between the two

	$C$	$n$	$R^2$
(4.11)	0.8076	0.8408	0.9869
(4.12)	0.7792	0.8356	0.8704

**Table 4.6:** Coefficients  $C$  and  $n$  provided in [4]

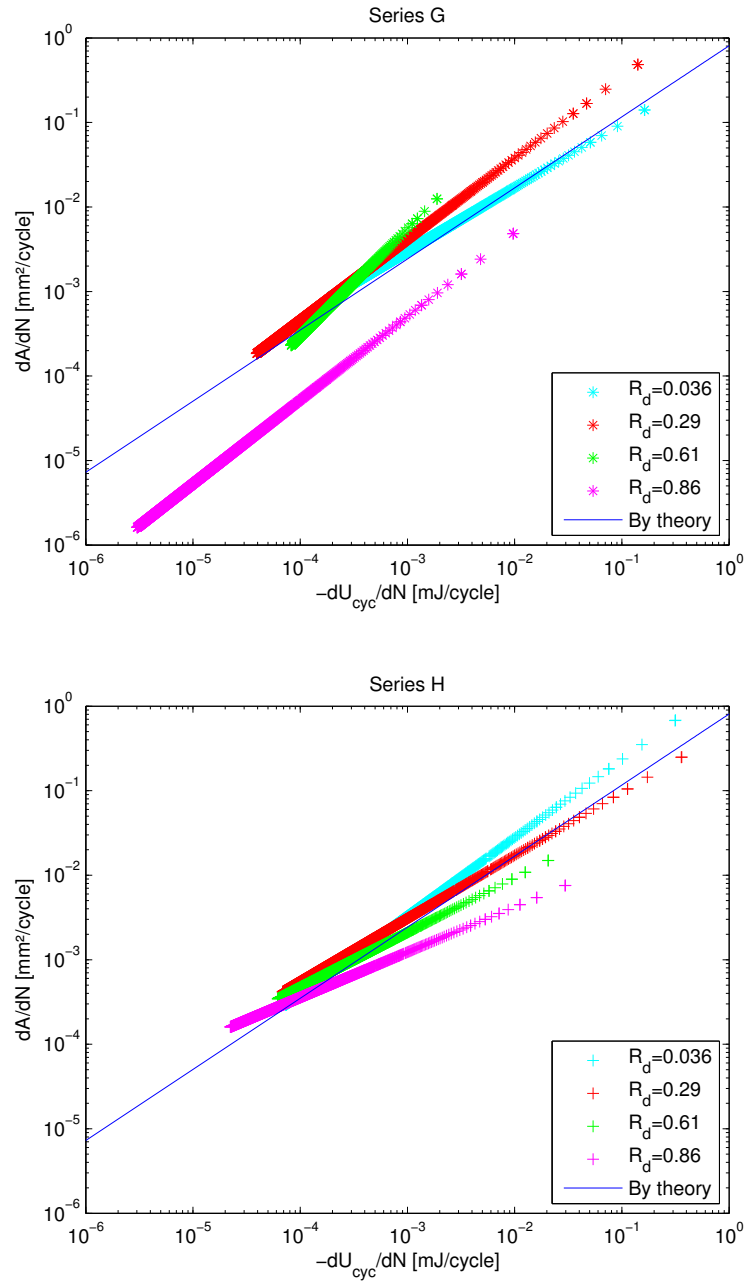


**Figure 4.13:** Logarithmic plot of  $\frac{dA}{dN}$  against  $\frac{dU_{cyc}}{dN}$

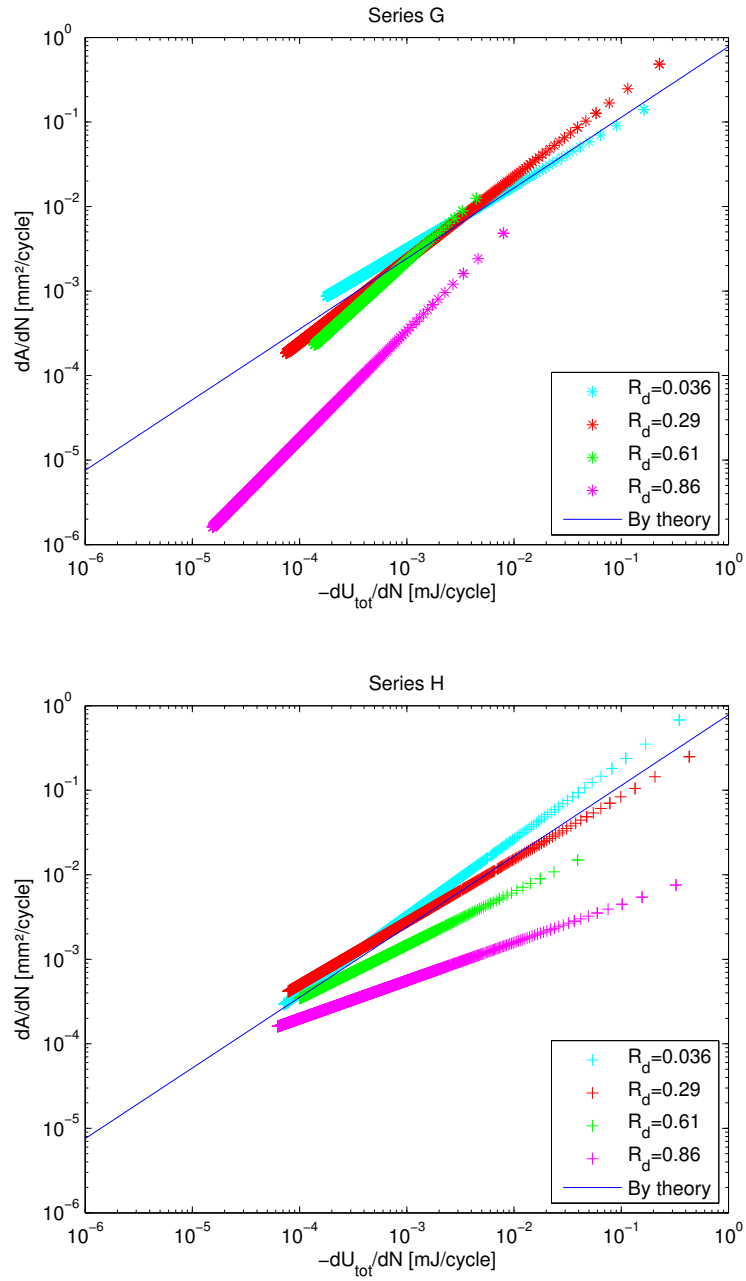


**Figure 4.14:** Logarithmic plot of  $\frac{dA}{dN}$  against  $\frac{dU_{tot}}{dN}$

	Series	$C$	$n$	$R^2$
(4.11)	G	1.514	0.8975	0.7343
	H	1.127	0.8562	0.8048
(4.12)	G	1.605	0.9638	0.9004
	H	0.7228	0.8480	0.5808

**Table 4.7:** Coefficients  $C$  and  $n$  computed according to tests

batches of specimens. The outcomes are collected in Table 4.7. The value of  $R^2$  is such that none of the two correlations proves to be clearly superior to the other. As far as concerns series G, considering the loss of total energy  $\frac{dU_{tot}}{dN}$  shows better results than employing the loss of cyclic energy  $\frac{dU_{cyc}}{dN}$ ; for series H it is quite the opposite.

Comparing the available data to the lines drawn according to [4] shows a good accordance with the expected behaviour. On the other hand the fitting curves obtained on the basis of the experimental data are quite similar to those computed by Pascoe et al. The reason for the slight variation in the slope  $n$  between different curves is not clear. It is possible that it is due to the technique employed for crack measurement or to that used for the computation of the strain energy. Apart from these small differences, the experimental data almost collapse on the line, with the most remarkable exception of data concerning tests at very high R-ratio. As expected, the results obtained for  $R_d = 0.86$  exhibit a significant deviation from the others, up to one order of magnitude in the value of the crack growth rate. This ought to be traced to the inaccuracy in measuring a very small crack growth.

Globally, the results do not show a net dependence on the R-ratio, that supports the validity of the energetic approach. As far as concerns the influence of the adhesive thickness, no substantial difference has been identified between the specimens belonging to series G and those belonging to series H. The magnitude of the deviation between data concerning different batches is so tiny that it could be due to data scattering; within the limits of this study, there is no evidence that the thickness of the adhesive layer has an effect on crack growth under fatigue loading.

## 4.7 Crack growth rate in quasi-static tests

The quasi-static tests have been performed with the aim of clarifying the question about the influence of the adhesive thickness. In this sense the following can be seen as a prosecution of the previous section. Similarly to

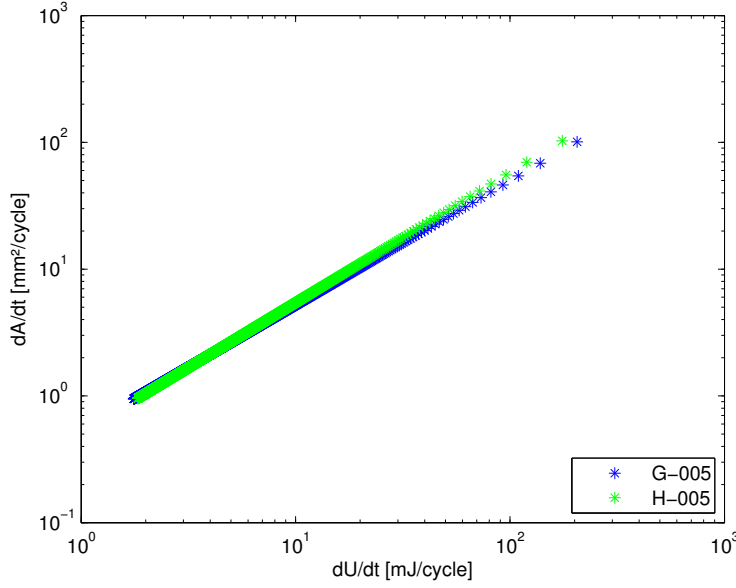


**Figure 4.15:** Correlation between  $\frac{dA}{dt}$  and  $\frac{dU}{dt}$

the approach used for fatigue, the amount of crack growth in a given time interval is related to the energy release in that interval. In Figure 4.15 is shown the correlation between  $\frac{dA}{dt}$  and  $\frac{dU}{dt}$ . The area of crack growth  $A$  is computed from the crack length under the hypothesis of straight crack front. This leads to  $\frac{dA}{dt} = w \frac{da}{dt}$ , being  $w$  the width of the specimen and  $a$  the crack length.

The lines relating to specimens belonging to different batches overlap almost perfectly. Although quasi-static testing has been performed only on an exiguous number of samples, this result somehow suggests that the influence of the thickness of the adhesive layer on crack growth is hardly quantifiable, at least under quasi-static loading. As far as concerns this topic, the experimental research performed does not provide further results.

We have computed the strain energy release rate by means of the MBT method as shown in section 4.5; in Figure 4.16 the crack growth rate is related to the SERR. Only values corresponding to  $t \geq 260$  s have been taken into account. This plot is useful for the evaluation of the fracture toughness.

A detailed study concerning the adhesive thickness under quasi-static loading conditions could lead to interesting results. We will address this question in the following by means of numerical simulations.

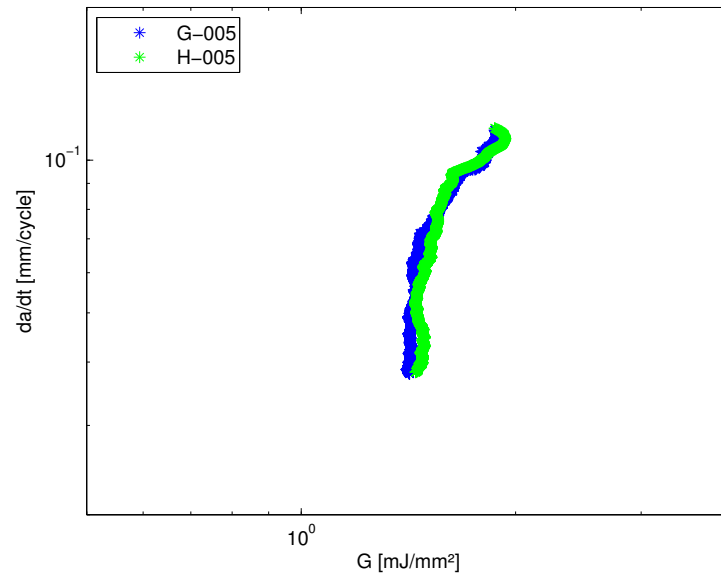


**Figure 4.16:** Logarithmic plot of  $\frac{da}{dt}$  against the SERR

# Chapter 5

## Numerical simulations

This chapter deals with a numerical approach to fracture of adhesive bonded joints. Our analysis focuses on simulations of the crack growth under quasi-static loading. First the theoretical background behind the numerical model employed is provided (see [2], [3] and [7] as references). Its implementation is then described and the results are shown.

### 5.1 Introduction to Cohesive Zone Models

*Cohesive Zone Models (CZM)* are a class of models developed in the field of fracture mechanics. Their origin dates back to the works by Elliott (1947), Barenblatt (1959), Dugdale (1960) and others; these models are gaining increasing interest as an alternative to other approaches to fracture mechanics like those based on LEFM (Linear Elastic Fracture Mechanics) or on CTOD (Crack Tip Opening Displacement). Compared to other methods, CZM provide several advantages:

- they can be applied to the analysis of uncracked structures, for instance to predict delamination in composites or disbonding in adhesive layers;
- nonlinear zones can be taken into account rejecting the hypothesis that they are confined in a small region;
- progressive damage of the material is considered through the deterioration of its properties;
- they are able to predict multiple cracking and allow mixed-mode behaviour.

Cohesive models assume that fracture takes place into a region comprised between two fictitious surfaces, called cohesive zone. The cohesive zone is

usually considered to be of zero thickness. For this reason CZM are particularly appropriate for situations in which an extremely thin layer must be modelled. Fracture is represented by the separation of the virtual surfaces. Basically, some traction forces are generated into the cohesive zone and resist to separation. The fracture process is linked to the decrease of the traction strength in the cohesive region. Complete separation occurs when the strength becomes zero.

The behaviour of the cohesive region is usually formulated in terms of traction-separation laws. The kernel of the cohesive zone is the relationship between the displacement of the fictitious surfaces and the traction that resists that separation. Cohesive models differ from each other depending on the particular form chosen for that relationship. A common feature to most CZM is that the traction-separation law can be subdivided in two distinct parts. Initially traction follows an increasing trend and opposes separation. At a given point a threshold is reached, that is the maximum traction and defines the onset of the damage process. It is the stress at which the crack is created. After that threshold, damage evolution occurs; as a consequence of material softening the traction starts decreasing. The points where a zero value is reached define the crack tip.

Choosing the particular function to represent the traction-separation law does not yield a unique result. As a matter of fact several different functions have been proposed over the years; among them linear, exponential, polynomial and trapezoidal ones are the most common. Whatever form one chooses for the law, some parameters must be specified with care:

- the threshold value of the traction, also referred to as cohesive strength;
- the displacement, called characteristic length, at which that maximum traction is reached;
- an additional parameter which uniquely defines the point at which complete separation occurs.

The cohesive strength is usually related to the yield stress of the material involved. Provided a form for the function has been chosen, the characteristic length can be computed from the cohesive strength by means of the inverse function. The characteristic length is a measure of the brittleness of the material; the bigger it is, the more ductile is the material. As far as concerns the last parameter, complete fracture could be related either to a maximum admissible value of the displacement, either to the energy dissipated in the fracture process. This choice is strongly linked to the physics of the problem. Relating the damage to the displacement means that complete separation occurs when the limit value of the displacement between

the two virtual surfaces is exceeded. This automatically fixes the end point of the traction-separation curve. On the other hand fracture can be related to energy dissipation; complete separation takes place when a critical value, i.e. the fracture energy, is reached. This energy is equal to the area below the traction-separation curve. The value of the fracture energy is mode-dependent. It is possible computing a mixed energy that can be used to predict damage evolution under mixed-mode loading conditions. Attention must be paid in the formulation of CZM so that only traction stresses trigger damage evolution, while compressive forces do not.

In the following we shall deal in detail with a cohesive zone model based on a linear traction-separation law. This is the same model that we have implemented in the simulations and it is useful having a good understanding of all the parameters involved. The traction-separation law employed is shown in Figure 5.1. The initial segment follows a linear elastic behaviour up to the point of damage initiation. The linear behaviour is formulated in terms of stress-strain relations expressed in matrix form. This formulation is especially suitable for the implementation in finite element methods. An orthogonal frame of reference is defined and the three mutually perpendicular directions are called  $n$ ,  $s$  and  $t$ , respectively aligned with the normal traction and with the two shear tractions. The nominal stress vector  $\boldsymbol{\sigma}$  is made up of the force components divided by the area of the undeformed cohesive element. The nominal strain vector  $\boldsymbol{\varepsilon}$  is made up of the strain components, which are computed according to:

$$\varepsilon_n = \frac{\delta_n}{T} \quad \varepsilon_s = \frac{\delta_s}{T} \quad \varepsilon_t = \frac{\delta_t}{T}$$

where  $\delta_n$ ,  $\delta_s$  and  $\delta_t$  are the components of the displacement between the virtual surfaces and  $T$  is the thickness of the elements. In finite element methods it is often assumed  $T = 1$ , which results in the strain being equal to the displacement. The components of the elastic modulus along the three directions form the constitutive matrix  $\mathbf{K}$ , which is symmetric. The stress-strain relations can be written as:

$$\boldsymbol{\sigma} = \begin{bmatrix} \sigma_n \\ \sigma_s \\ \sigma_t \end{bmatrix} = \begin{bmatrix} K_{nn} & K_{ns} & K_{nt} \\ K_{sn} & K_{ss} & K_{st} \\ K_{tn} & K_{ts} & K_{tt} \end{bmatrix} \begin{bmatrix} \varepsilon_n \\ \varepsilon_s \\ \varepsilon_t \end{bmatrix} = \mathbf{K}\boldsymbol{\varepsilon}.$$

The figure deals with the case of pure normal traction. Considering traction along the shear directions would yield a similar plot, with the only expedient of replacing subscript  $n$  with  $s$  or  $t$  respectively. The characteristic length is denoted by  $\delta_n^0$ . It corresponds to the cohesive strength  $\sigma_n^0$ . Several different criteria can be adopted to describe damage initiation, usually based

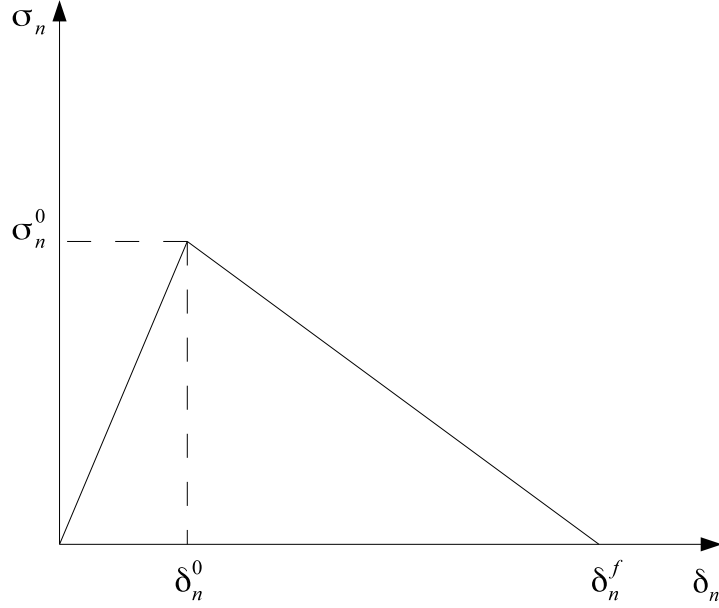


**Figure 5.1:** Plot of the linear traction-separation law

on the ratio between applied and peak stress or on the ratio between strains. Among them:

- maximum nominal stress criterion:  $\max \left\{ \frac{\sigma_n}{\sigma_n^0}, \frac{\sigma_s}{\sigma_s^0}, \frac{\sigma_t}{\sigma_t^0} \right\} = 1$ ;
- maximum nominal strain criterion:  $\max \left\{ \frac{\varepsilon_n}{\varepsilon_n^0}, \frac{\varepsilon_s}{\varepsilon_s^0}, \frac{\varepsilon_t}{\varepsilon_t^0} \right\} = 1$ ;
- quadratic nominal stress criterion:  $\left( \frac{\sigma_n}{\sigma_n^0} \right)^2 + \left( \frac{\sigma_s}{\sigma_s^0} \right)^2 + \left( \frac{\sigma_t}{\sigma_t^0} \right)^2 = 1$ ;
- quadratic nominal strain criterion:  $\left( \frac{\varepsilon_n}{\varepsilon_n^0} \right)^2 + \left( \frac{\varepsilon_s}{\varepsilon_s^0} \right)^2 + \left( \frac{\varepsilon_t}{\varepsilon_t^0} \right)^2 = 1$ .

In our model the maximum nominal stress criterion has been employed.

Damage evolution describes the softening of the material. The damage is represented by a quantity called  $D$ . Its initial value is equal to 0, indicating that the material is undamaged; once damage initiation is reached,  $D$  increases monotonically up to 1, which corresponds to complete fracture. The stress-strain relations become:

$$\boldsymbol{\sigma} = (1 - D)\mathbf{K}\boldsymbol{\varepsilon}.$$

For linear softening the damage is computed as:

$$D = \frac{\delta_m^f (\delta_m^{max} - \delta_m^0)}{\delta_m^{max} (\delta_m^f - \delta_m^0)}$$

where  $\delta_m = \sqrt{\delta_n^2 + \delta_s^2 + \delta_t^2}$  is the effective displacement,  $\delta_m^{max}$  is the maximum value that it attains due to loading and  $\delta_m^f$  is the value at which total failure takes place.

As far as concerns failure, we assume an energetic criterion: complete fracture occurs when the critical energy  $\mathcal{G}_c$  is reached. In the case of a linear curve the maximum separation under normal traction can be computed simply:

$$\delta_n^f = \frac{2\mathcal{G}_c}{\sigma_n^0}.$$

## 5.2 Implementation of the numerical model

A numerical model has been developed to analyse the behaviour of the DCB specimens from the two different batches under quasi-static loading. A Finite Element Method (*FEM*) has been employed for modelling. The nature of the real specimens requires to consider two key features. First of all the model needs to take into account properly the adhesive bond between the top beam and the bottom one. Since the aim of the simulations is predicting the crack growth into the adhesive layer, a numerical model should be used that is able to represent the fracture of the adhesive bond. The cohesive zone model discussed in the previous section is an eligible candidate to model the adhesive. The second characteristic of the model concerns the value of the adhesive thickness. In most cases the thickness of the adhesive is negligible and the cohesive region is assumed to have zero thickness. Being the comparison between specimens with different thickness one of the major objects of the simulations, we need to deal with the adhesive thickness as a main component of our model.

Three different configurations have been taken into consideration for modelling, provided in Figure 5.2:

- Configuration (a): shown in 5.2a, the aluminium beams are modelled by elements 1, the adhesive layer is represented by a zero-thickness cohesive zone model, denoted by the red line in figure. Since this configuration does not take into account the thickness of the adhesive, it is not suitable for complete simulations; on the other hand it is a useful first step towards more complex models.
- Configuration (b): shown in 5.2b, the aluminium beams are modelled by elements 1 as in the previous model; the adhesive layer is now composed by two distinct elements. The thickness is provided by elements

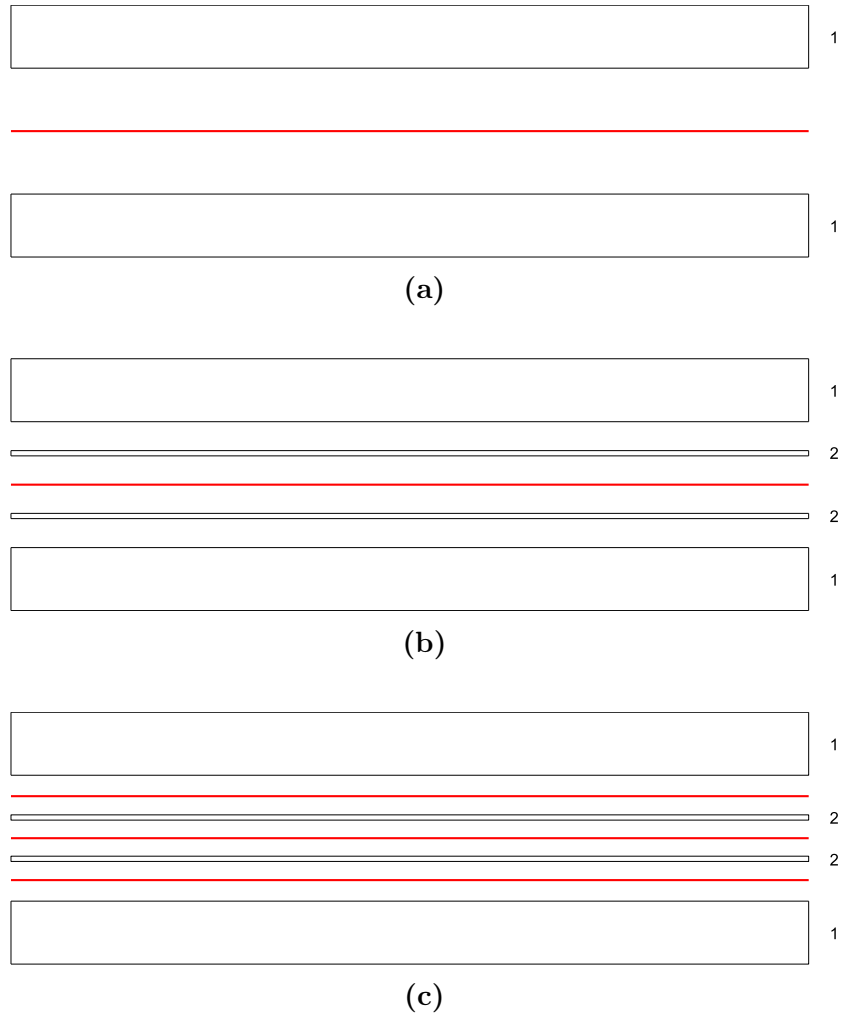


**Figure 5.2:** Configurations considered for the development of the model

2: they are symmetric and the thickness of each of them is equal to the average adhesive thickness measured in the actual specimens. These elements are made of epoxy and follow an elastic-plastic behaviour. The bonding function of the adhesive is modelled by a cohesive zone model (red line) with zero thickness. This configuration is more refined than the previous one and takes into account both the features required for the simulations. It is based on the assumption that cracking occurs along the mid-line of the adhesive; failure at the aluminium-epoxy interface is not taken into account.

- Configuration (c): shown in 5.2c, it is based on the previous configuration, with the addition of two cohesive layers at the aluminium-adhesive interfaces. This modification allows to consider crack propagation both into the adhesive and along the interfaces. Its main limitation is the inherent complexity.

Configuration (b) has been selected for simulations. It seems to be the best trade-off between performance and complexity. Additionally it is consistent with the outcomes from numerical testing, which exhibit failure into the adhesive instead of at the adherend-adhesive interface. As a first step, configuration (a) has also been implemented to gain preliminary knowledge of the numerical model. The models have been implemented on the software *Abaqus/Standard*. Because of the complexity of the problem, the attempts made to run 3D simulations faced severe convergence issues. As a consequence 2D models have been implemented.

The mesh of the model is not homogeneous. Quadrangular elements have been employed on the whole domain, with different sizes depending on the meshed part. A relatively coarse mesh has been used for the aluminium beams, with a spacing between the meshing elements equal to 1 mm. The epoxy layers are 0.15 mm thick in series G and 0.10 mm thick in series H. Thus they require a fine mesh and a spacing of 0.05 mm has been used. Concerning the cohesive layer, a thickness equal to  $10^{-3}$  mm is used, which is in line with the theoretical zero thickness. Meshing elements with a spacing of 0.5 mm and 0.05 mm have been compared. The value of the spacing has been found to strongly affect the stability of the model. Using a 0.5 mm wide spacing causes stresses computed into the epoxy layers (with a finer grid) to concentrate around the nodes of the cohesive elements, thus giving rise to stress peaks that are possibly responsible for convergence issues. A spacing equal to 0.05 mm basically provides matched meshes across the epoxy-cohesive interface and allows for a smoother stress distribution. This value has finally been employed in the simulations. Surface-based tie constraints have been used to bind together the components of the model.

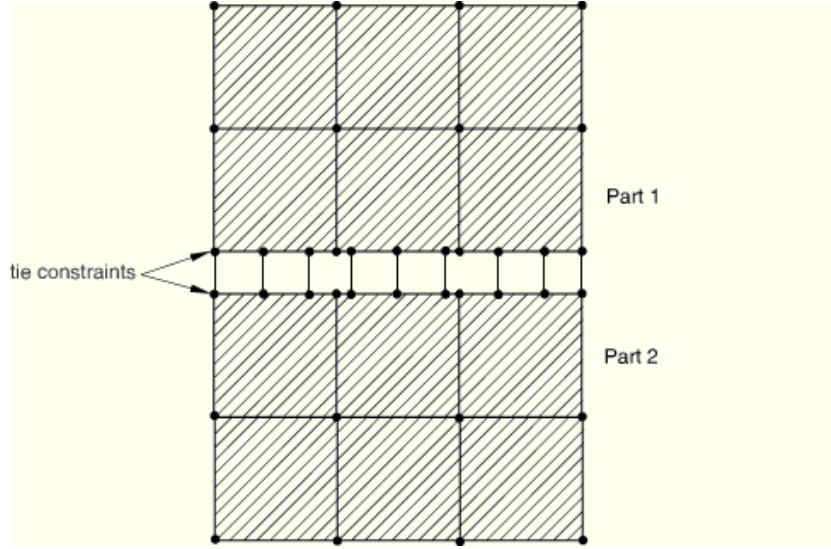


**Figure 5.3:** Tie constraints between surfaces (image based on [7])

	$E$ [GPa]	$\nu$	$\sigma_Y$ [MPa]
Al-2024-T3	73.1	0.33	320
FM94	3.0	0.35	20

**Table 5.1:** Mechanical properties used in the model

They are shown in Figure 5.3. By means of these constraints it is possible to tie together parts with unmatched meshes, like at the aluminium-epoxy interface.

Both the aluminium and the epoxy have been described as isotropic elastic-plastic materials. Their behaviour is linear elastic up to the yielding point, after which plastic deformation occurs. The nonlinear plastic behaviour has been characterised by a sequence of points provided by data sheets. The parameters concerning the mechanical properties of the aluminium and of the epoxy have been taken from data sheets and are collected in Table 5.1.

The FM94 data sheet provides no information concerning the methodology employed to measure the properties of the adhesive; moreover some properties are completely missing. The evaluation of the properties needed to characterise the traction-separation law is a critical point of the model implementation. The stability of the numerical algorithm depends on the values of the mechanical properties and so do the results. We have assumed  $\sigma_n^0$  to be equal to the ultimate stress provided by the FM94 data sheet. The

following values of the cohesive strength have been used:  $\sigma_n^0 = 50$  MPa and  $\sigma_s^0 = \sigma_t^0 = 30$  MPa. As far as concerns the constitutive matrix, we have considered the case of decoupled traction, thus  $K$  becomes a diagonal matrix:  $K_{ns} = K_{nt} = K_{st} = 0$ . The elements on the diagonal strongly influence the results and since exact data for their determination are not available, in the next section we will show results obtained with different values of  $K_{nn}$ ,  $K_{ss}$  and  $K_{tt}$ . The fracture energy can be evaluated according to the outcomes from quasi-static testing provided in section 4.7. This gives  $\mathcal{G}_c = 1.7$  N/mm as a result. In the model both this value and a virtual value  $\mathcal{G}_c = 2.5$  N/mm have been used.

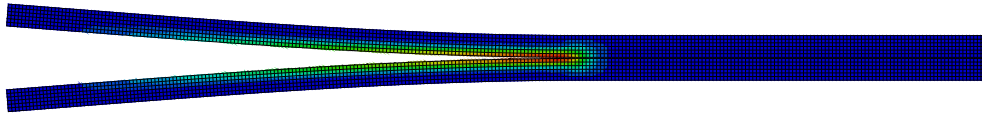
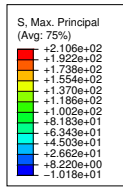
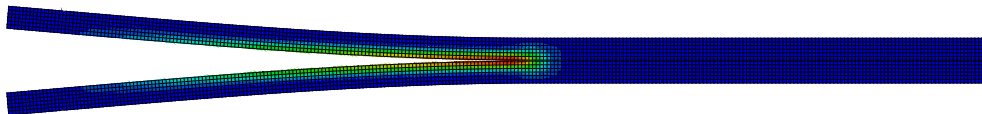
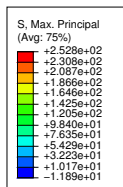
### 5.3 Numerical results

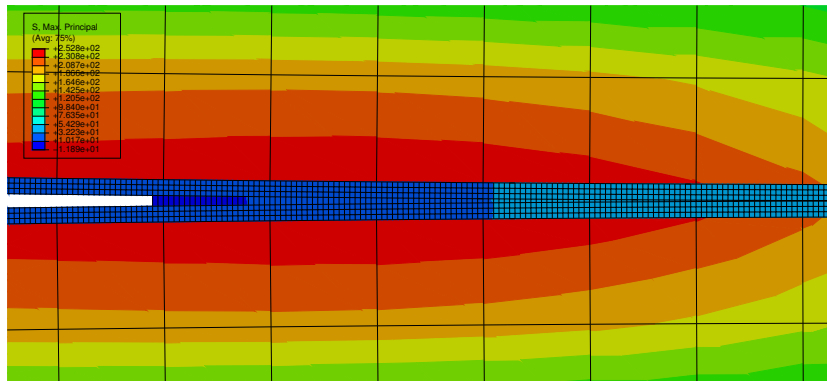
In the following we will show the results of the numerical simulations. The developed models prove to be able to predict crack growth under quasi-static conditions. The value of the fracture energy directly affects crack propagation. Figure 5.4 shows the different outcomes of simulations on a series G specimen using  $\mathcal{G}_c = 1.7$  N/mm and  $\mathcal{G}_c = 2.5$  N/mm. The diagonal elements of the constitutive matrix have been assumed to be  $K_{nn} = 28$  GPa and  $K_{ss} = K_{tt} = 14$  GPa. The images refer to the point of maximum applied displacement, namely  $d = 15$  mm. The final crack length computed in the two cases is  $a_{num} = 155$  mm for  $\mathcal{G}_c = 1.7$  N/mm and  $a_{num} = 143$  mm for  $\mathcal{G}_c = 2.5$  N/mm. These values are close to the length  $a_{exp} = 140$  mm measured from experimental testing. The higher fracture energy results in a crack length that is closer to the measured value. As expected from testing, stresses in the aluminium beams do not exceed the yielding point.

As stated in the previous section, different simulations have been performed with different values of the elements of matrix  $\mathbf{K}$ . According to their results, the final crack length is basically unaffected by the choice of the matrix. On the other hand, the components of the constitutive matrix, i.e. the stiffness of the cohesive layer, influence the stress distribution around the crack tip. Figure 5.5 illustrates the stress field obtained with different values of the stiffness. The values used in the two cases are shown in Table 5.2,

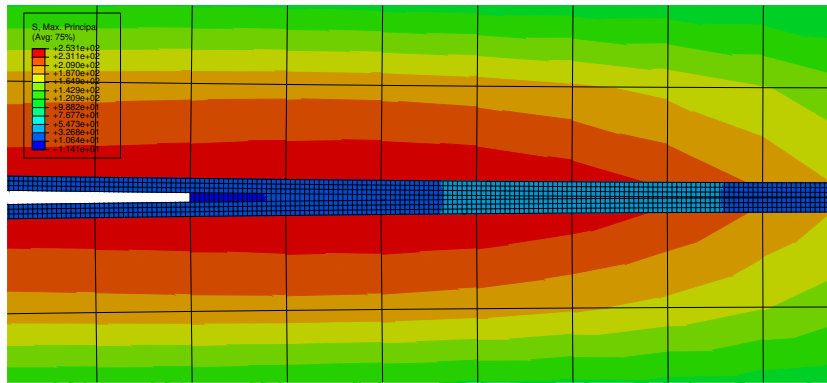
	$K_{nn}$ [GPa]	$K_{ss}$ [GPa]	$K_{tt}$ [GPa]
(a)	28	14	14
(b)	3	1.2	1.2

**Table 5.2:** Elements on the main diagonal of matrix  $\mathbf{K}$

(a)  $\mathcal{G}_c = 1.7 \text{ N/mm}$ (b)  $\mathcal{G}_c = 2.5 \text{ N/mm}$ **Figure 5.4:** Effect of fracture energy on crack growth



(a) High stiffness

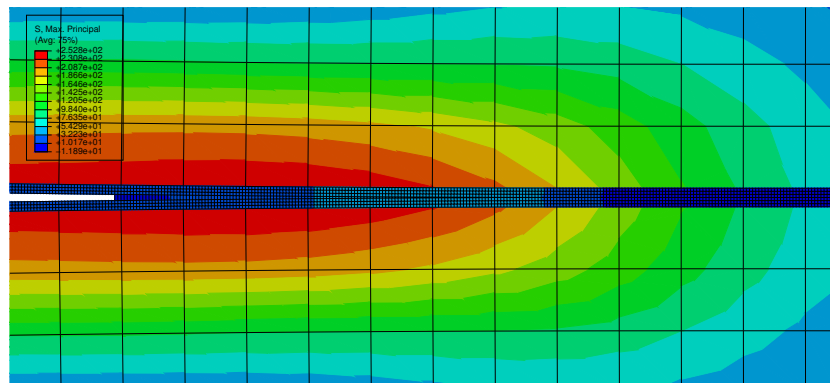


(b) Low stiffness

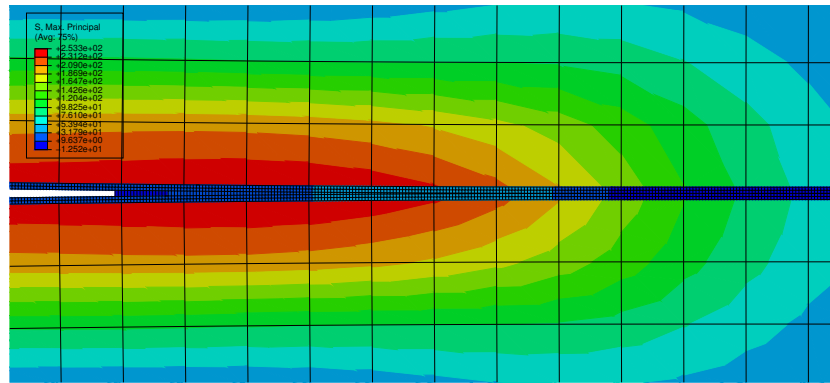
**Figure 5.5:** Effect of cohesive stiffness on the stress distribution

denoted after their corresponding figures. In both simulations the fracture energy is  $\mathcal{G}_c = 2.5$  N/mm. The maximum stress attained in the two cases is approximately the same. However, in the case with higher stiffness the stresses are generally higher both in the adhesive and in the aluminium. In particular, the region of stress concentration around the crack tip is slightly larger.

The main result from numerical simulations is the comparison between specimens from series G and from series H. According to the findings explained above, a value of the fracture energy  $\mathcal{G}_c = 2.5$  N/mm has been chosen for the simulations of specimens of both batches. Although this value is higher than the one measured from tests, it provides a prediction of the



(a) Series G

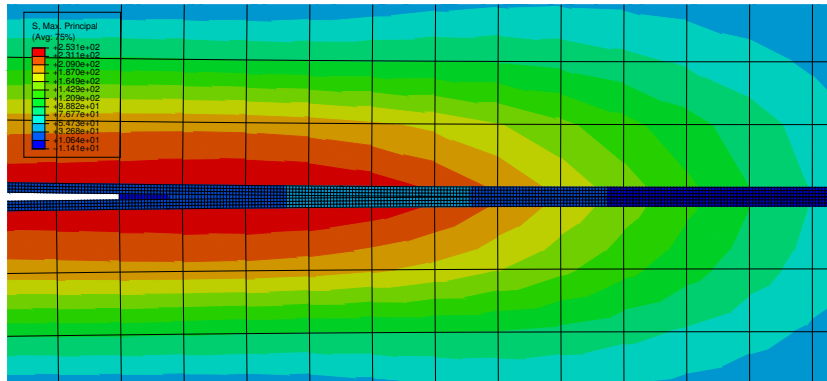


(b) Series H

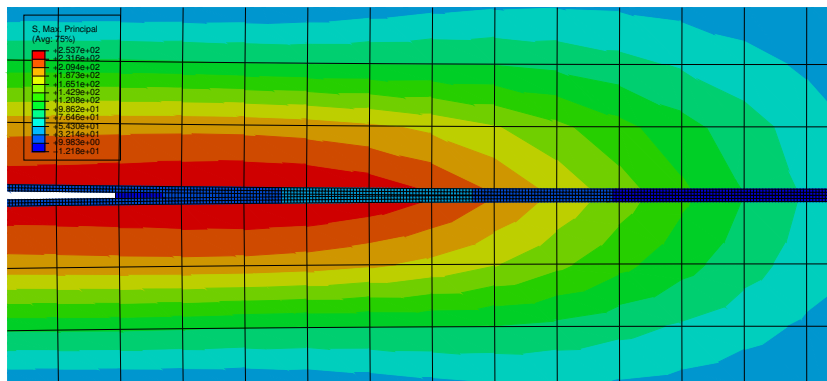
**Figure 5.6:** Stress field, in case of high cohesive stiffness

crack length that is extremely close to reality. As far as concerns  $\mathbf{K}$ , are shown results concerning both the case with high cohesive stiffness and the one with low cohesive stiffness. See Table 5.2 for the values employed for the elements of the matrix. Specimens of the two batches are compared in Figure 5.6 and 5.7, respectively in the case with high stiffness and in that with low stiffness.

Results obtained in the two cases are similar, evidencing that little contribution comes from the value of the cohesive stiffness. The simulations show the presence of high stresses about the crack tip. A net discontinuity in the stress field occurs at the adherend-adherent interface, due to the one order of magnitude difference in elastic modulus of aluminium and of epoxy. Stresses



(a) Series G



(b) Series H

**Figure 5.7:** Stress field, in case of low cohesive stiffness

in aluminium are under the yield stress of Al-2024-T3, meaning that no plastic effect occurs in the top and bottom beams. Conversely, the stresses in the light blue region in the adhesive reach values as high as 45 MPa, far beyond the yielding point of FM94, which is about 20 MPa at room temperature. As a consequence, a plastic zone is created ahead of the crack tip. This region is responsible for energy dissipation. Globally the figures do not evidence significant differences in the stress distribution between series G and series H. Small differences are observed in the local values of the stresses into the adhesive ahead of the crack tip; in particular the stresses are slightly higher in case of series H. The reason for this is possibly due to the fact that the cross-sectional area of the adhesive in series H is smaller than in series G, causing increased stress concentration. Higher stresses account for a bigger amount of energy dissipated by plasticity. The evaluation of total plastic energy dissipation must however consider that the plastic zone is actually larger in series G. In fact the adhesive length affected by plasticity is approximately the same in the two batches, but the adhesive is thicker in series G, resulting in a larger area. As a result, the energy dissipation associated to plasticity in both batches is much the same. This outcome is in line with the results of experimental tests, which do not evidence differences between specimens from series G and series H.

# Chapter 6

## Conclusions

The present thesis has dealt with the subject of adhesively bonded joints. In particular, aluminium-epoxy DCB specimens under Mode I loading have been studied. The main object has been the determination of the influence of the adhesive thickness on adhesive cracking under fatigue loading. This research study has been conducted by means of experimental testing on specimens from two different batches. The two series of specimens, namely series G and series H, differ by the average value of the adhesive thickness, which is higher in the former batch. Eight fatigue tests have been performed on eight specimens, four per each series. In addition to fatigue tests, two quasi-static tests have also been performed on specimens from both batches to provide data on crack growth. Crack measurement has been taken by means of a camera.

The crack growth rate has been obtained from data concerning the crack length. The energy release associated to crack growth has then be computed, both on a *per crack length* basis and on a *per cycle* basis. Computing the energy release per unit crack length, i.e. involving the derivative  $\frac{d}{da}$ , has led to the definition of SERR. The correlation curves between the crack growth rate and the strain energy release rate have been plotted. They show a dependence on the R-ratio. An alternative approach has been carried out, based on the computation of the energy release per unit cycle, i.e. involving the derivative  $\frac{d}{dN}$ . The crack growth rate has been related to the energy release rate per cycle. The resulting curves do not show a net dependence on the R-ratio. Curves relating to specimens from different batches are similar; moreover they match well the results of [4]. This suggests that the adhesive thickness has little influence on crack growth under fatigue loading. As far as quasi-static tests are concerned, both the SERR and the instantaneous energy release have been computed and related to the crack growth rate. The outcomes show basically no dependence on the adhesive thickness.

Besides experimental tests, a 2D finite element model has been developed to simulate the behaviour of the specimens under quasi-static loading. Cohesive Zone Models (CZM) have been employed to model crack propagation in the adhesive layer. The model has been implemented on *Abaqus/Standard*. The crack length predicted by the model matches well the outcomes of the tests. The numerical simulations have provided results about the stress distribution into the specimens and in particular into the adhesive. They have evidenced the creation of a plastic zone about the crack tip. This region is restricted to the adhesive and is a source of energy dissipation. A comparison between simulations referring to the two batches has shown small differences in the plastic zone. The amount of energy dissipation in both cases is expected to be much the same.

The results of this research study suggest that an energetic approach is appropriate to describe fatigue crack growth in adhesively bonded joints. In particular, relating crack growth to energy release produces R-ratio independent curves when both quantities are considered per cycle. This supports the idea that, being fatigue a cyclic phenomenon, crack growth under fatigue loading should be evaluated considering the quantities involved at each single cycle. The energy release, evaluated per cycle, seems able to completely characterise the crack growth without the introduction of ad hoc parameters.

Experimental results do not evidence a clear correlation between crack growth and adhesive thickness. Specimens from series G and from series H have produced similar outcomes both in fatigue and in quasi-static tests. A possible explanation for this is that the stresses about the crack are not much influenced by differences in the adhesive thickness. This hypothesis has been examined by means of numerical simulations. Indeed, their results show little variations of the stress field in the two batches; the plastic zone differs little as well. The outcomes from experiments and those from simulations fit well together. The conclusion of this study is that the adhesive thickness does not substantially influence crack growth.

Further developments could be carried out on this subject. Additional testing could be led, taking into consideration specimens with larger values of the adhesive thickness. In particular, more quasi-static tests could be performed and their results compared to those shown in the present study. Developments of the techniques used for crack measurement might provide the analysis with more accurate data. As far as concerns numerical simulations, a 3D model could be developed and fatigue loading could be considered. The convergence problems that have been encountered during the implementation of a 3D model might be tackled by using *Abaqus/Explicit*. Finally, experiments should be conducted to better characterise the mechanical properties of the FM94 resin and improve the data used in the simulations.

# Appendix A

## Specimen data

In section 3.1 the manufacturing process of the specimens has been described, together with their size and the technique used to measure them. For sake of clarity it has been deemed preferable to omit some details concerning the procedure employed to select the specimens used for testing, as well as the full set of data and pictures acquired from the measurement session. In the following the necessary additions will be provided to the reader.

ASTM Standard D5528 prescribes a given size for the specimens, which represents a nominal value. Of course this size can not be exactly achieved by manufacturing, that leads to the need for measurements. The measurement instrumentation has already been addressed; it is now interesting to look in detail what data have been acquired and how they have been analysed. The microscope and its acquisition software basically have provided pictures like the one in Figure 3.4, showing the adhesive layer and its interface with the adherents at a microscopic level. By means of the software it is also possible to take a measurement of the thickness of the intermediate film at different points directly from the picture. This is basically achieved by the elaboration program counting the pixels and considering the applied magnification factor to relate them to the physical dimensions of the object. One picture has been taken at each station of every specimen. The number of points at which the measurement has been performed varies from one picture to another, generally being around three and raising up to six in a couple of cases (see Figure A.2a).

This is a direct consequence of the different level of roughness in different pictures and of the attempt to estimate the variation between the highest and the lowest value of the local thickness rather than its average value. The "average" thickness has subsequently been computed as the mean between these two values, the error being the distance from the mean. This arbitrary choice may be questionable, but it should be noticed that for a reliable com-

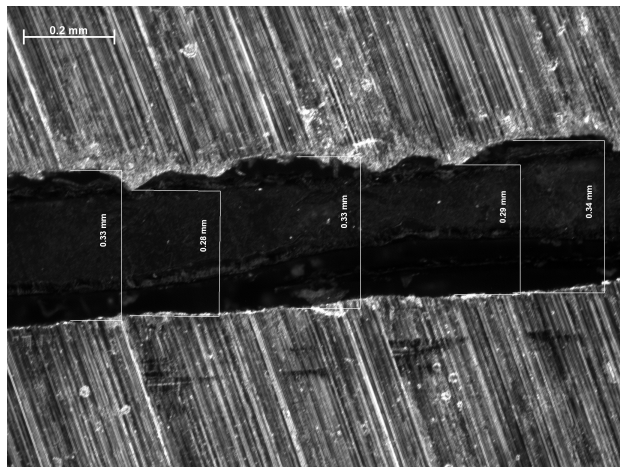
putation of the average value in its usual definition, it should undoubtedly be meant as a weighted average, that would imply the knowledge of the actual distribution of thickness. Because of the complexity of this issue, the alternative approach has been preferred.

It has already been pointed out that measurements at stations A, B and C yield different results, showing that the thickness is far from being constant along the length of the specimen. This phenomenon may be appreciated in an empirical fashion from a comparison between the pictures in Figure A.1, showing a specimen from series G, and between the pictures in Figure A.2, referred to a specimen from series H.

From location A to C, a decrease of the thickness to one half of its original value can be noticed, the most important variation occurring between sections B and C. The same trend is visible in all the specimens, irrespective whether they belong to batch G or H. Given that the stations are equispaced, it may be assumed that most of the variation is bounded near point C. Additional measurements have been taken to assess the validity and the limits of this assumption. For this purpose specimen G-005 have been measured at intermediate locations between B and C, spaced of 7.5 mm from each other, which, starting from point C, are denoted as C1, C2, C3 and C4. The results are shown in Figure A.3 starting from the midline. In addition to that, the thickness at station C is approximately the same for every specimen, frustrating the use of different types of specimens. Hence the choice to limit the length of the specimen that is valid for testing to a region far from location C.

Length, width and thickness of the specimens have been measured by means of a calliper. The results of the measurements are collected into tables, divided on account of the series. Table A.1 contains the dimensions of the specimens as measured by the caliper. In Tables A.2 and A.3 the values of thickness of the adhesive film at different points are given as taken from each picture (notice that the number of points is not constant), together with its average value and the error. Since data concerning the thickness at location C have been neglected, they are not included in these tables.

Although ten samples from each series were available, a smaller number of tests was scheduled. Because of that, it seems reasonable choosing those specimens, whose features fit best the ones required by the experimental activity; the collected data have been used to make a choice. As can be easily expected, the thickness of the adhesive layer has been the discriminating factor. Two parameters have been considered: the average value of the thickness itself and its variation along the length of the specimen. Since the main goal of the experiments is investigating the influence of the adhesive thickness on the propagation of cracks, it is convenient to isolate specimens with remark-



(a) Station A



(b) Station B

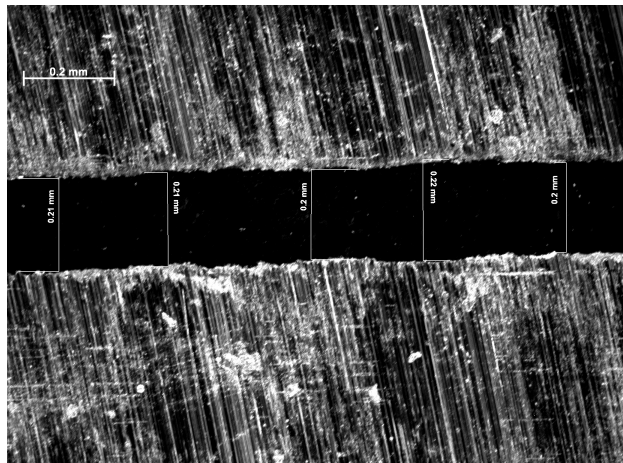


(c) Station C

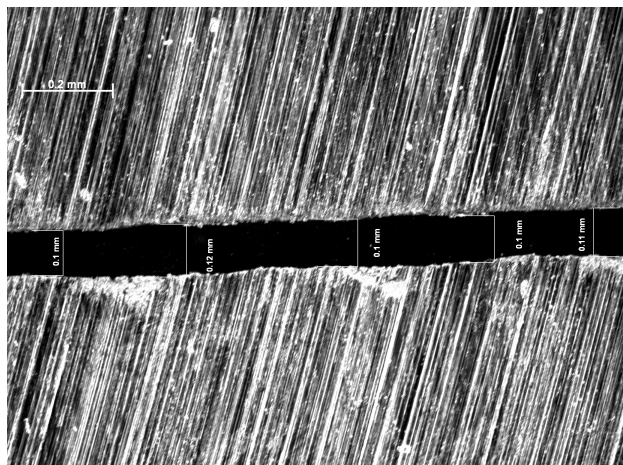
Figure A.1: Pictures from G-006 at different stations



(a) Station A

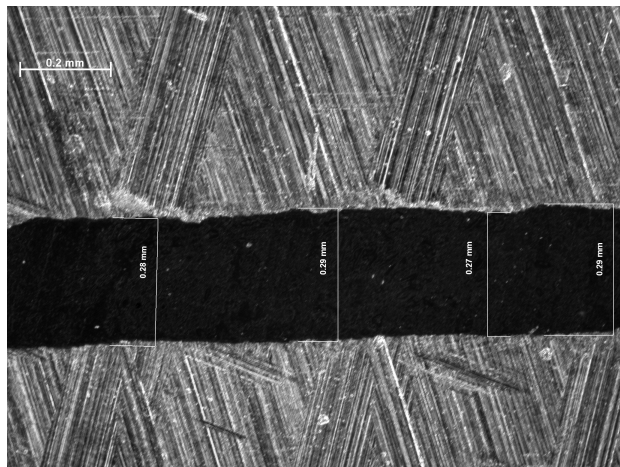


(b) Station B



(c) Station C

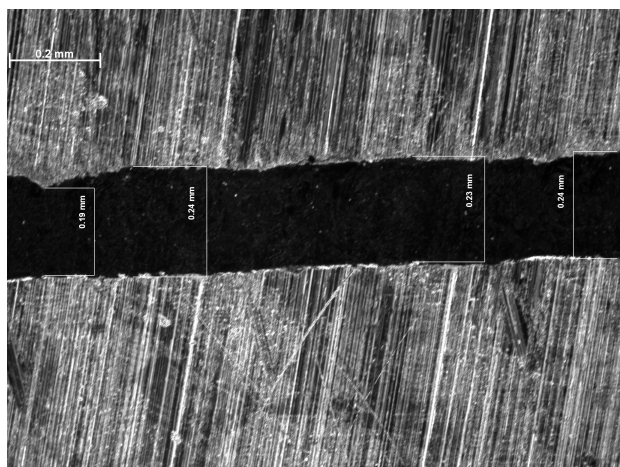
Figure A.2: Pictures from H-008 at different stations



(a) Section B



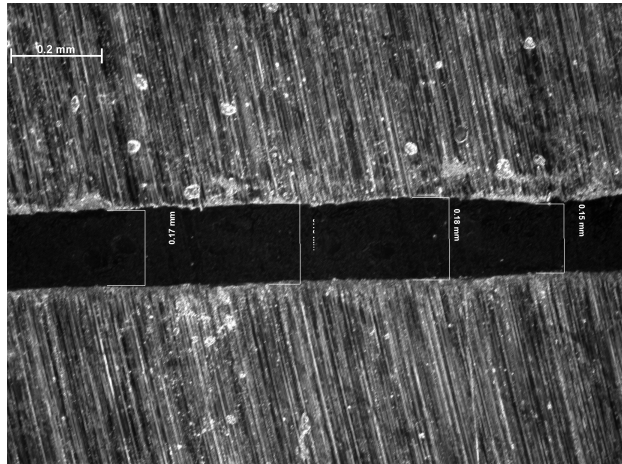
(b) Section C4



(c) Section C3



(d) Section C2



(e) Section C1



(f) Section C

**Figure A.3:** Pictures from G-005 at different sections

Type II	$L$ [mm]	$w_A$ [mm]	$t_A$ [mm]	$w_B$ [mm]	$t_B$ [mm]	$w_C$ [mm]	$t_C$ [mm]	$w_{avg}$ [mm]	$t_{avg}$ [mm]
G-001	272	24.96	12.54	24.97	12.43	25.03	12.38	24.99	12.45
G-002	272	24.97	12.47	24.98	12.44	24.97	12.29	24.97	12.40
G-003	271	24.98	12.48	24.97	12.32	25.07	12.29	25.01	12.36
G-004	272	25.02	12.46	24.97	12.34	25.05	12.24	25.01	12.35
G-005	272	24.99	12.51	24.98	12.43	24.99	12.31	24.99	12.42
G-006	272	25.09	12.59	25.01	12.43	25.22	12.31	25.11	12.44
G-007	272	25.19	12.49	25.04	12.38	25.08	12.32	25.10	12.40
G-008	272	25.00	12.49	24.99	12.42	24.99	12.31	24.99	12.41
G-009	272	25.10	12.49	25.03	12.39	25.06	12.34	25.06	12.41
G-010	272	25.05	12.48	25.02	12.42	25.04	12.29	25.04	12.40

Type III	$L$ [mm]	$w_A$ [mm]	$t_A$ [mm]	$w_B$ [mm]	$t_B$ [mm]	$w_C$ [mm]	$t_C$ [mm]	$w_{avg}$ [mm]	$t_{avg}$ [mm]
H-001	271	24.97	12.48	24.99	12.28	25.19	12.32	25.05	12.36
H-002	271	25.00	12.44	24.98	12.35	25.18	12.29	25.05	12.36
H-003	272	25.05	12.47	25.08	12.31	25.05	12.29	25.06	12.36
H-004	271	24.98	12.52	25.03	12.39	24.99	12.27	25.00	12.39
H-005	271	25.09	12.47	25.02	12.36	25.03	12.27	25.05	12.37
H-006	270	25.08	12.43	25.04	12.38	25.03	12.28	25.05	12.36
H-007	272	24.98	12.50	24.96	12.49	25.02	12.36	24.99	12.45
H-008	271	25.04	12.46	25.01	12.43	25.05	12.29	25.03	12.39
H-009	272	24.96	12.43	24.98	12.45	25.01	12.28	24.98	12.39
H-010	271	25.10	12.53	25.01	12.51	25.01	12.35	25.04	12.46

**Table A.1:** Length, width and thickness of specimens from series G and H

Type II	Thickness at A [ $mm$ ]					Average thickness [ $mm$ ]
G-001	0.29	–	–	–	–	0.290
G-002	0.34	0.24	0.33	0.29	–	$0.290 \pm 0.050$
G-003	0.26	0.33	0.23	0.28	–	$0.280 \pm 0.050$
G-004	0.30	0.32	0.35	0.29	–	$0.320 \pm 0.030$
G-005	0.33	0.28	0.27	0.32	–	$0.300 \pm 0.030$
G-006	0.33	0.28	0.33	0.29	0.34	$0.310 \pm 0.030$
G-007	0.31	0.28	0.25	0.29	–	$0.280 \pm 0.030$
G-008	0.26	0.33	0.28	0.32	0.29	$0.295 \pm 0.035$
G-009	0.27	0.33	0.32	0.26	0.31	$0.295 \pm 0.035$
G-010	0.31	0.29	0.30	0.28	–	$0.295 \pm 0.015$

Type II	Thickness at B [ $mm$ ]				Average thickness [ $mm$ ]
G-001	0.26	0.29	0.28	–	$0.275 \pm 0.015$
G-002	0.29	0.26	0.28	–	$0.275 \pm 0.015$
G-003	0.18	0.15	0.18	–	$0.165 \pm 0.015$
G-004	0.24	0.22	0.23	–	$0.230 \pm 0.010$
G-005	0.28	0.29	0.27	0.29	$0.280 \pm 0.010$
G-006	0.28	0.27	0.28	–	$0.275 \pm 0.005$
G-007	0.19	0.18	0.16	0.19	$0.175 \pm 0.015$
G-008	0.27	0.28	0.28	0.27	$0.275 \pm 0.005$
G-009	0.25	0.28	0.28	0.26	$0.265 \pm 0.015$
G-010	0.28	0.29	0.29	0.28	$0.285 \pm 0.005$

**Table A.2:** Thickness of the adhesive layer of series G specimens

Type III	Thickness at A [ <i>mm</i> ]						Average thickness [ <i>mm</i> ]
H-001	0.19	0.15	0.22	0.17	–	–	$0.185 \pm 0.035$
H-002	0.26	0.24	0.26	0.24	0.27	–	$0.255 \pm 0.015$
H-003	0.26	0.28	0.21	0.22	0.28	–	$0.245 \pm 0.035$
H-004	0.25	0.25	0.23	0.27	0.23	–	$0.250 \pm 0.020$
H-005	0.21	0.24	0.20	0.23	–	–	$0.220 \pm 0.020$
H-006	0.27	0.19	0.25	0.28	0.23	–	$0.235 \pm 0.045$
H-007	0.24	0.28	0.21	0.22	–	–	$0.245 \pm 0.035$
H-008	0.23	0.25	0.21	0.28	0.21	0.25	$0.245 \pm 0.035$
H-009	0.20	0.28	0.25	0.20	0.27	0.27	$0.240 \pm 0.040$
H-010	0.26	0.28	0.27	0.28	0.30	–	$0.280 \pm 0.020$

Type III	Thickness at B [ <i>mm</i> ]						Average thickness [ <i>mm</i> ]
H-001	0.10	0.07	0.07	0.09	–	–	$0.085 \pm 0.015$
H-002	0.19	0.20	0.20	0.20	–	–	$0.195 \pm 0.005$
H-003	0.14	0.14	0.13	0.14	–	–	$0.135 \pm 0.005$
H-004	0.25	0.26	0.23	0.26	0.26	–	$0.245 \pm 0.015$
H-005	0.13	0.13	0.12	0.13	–	–	$0.125 \pm 0.005$
H-006	0.23	0.21	0.22	0.21	0.21	–	$0.220 \pm 0.010$
H-007	0.32	0.29	0.30	0.33	–	–	$0.310 \pm 0.020$
H-008	0.21	0.21	0.20	0.22	0.20	–	$0.210 \pm 0.010$
H-009	0.28	0.27	0.28	0.30	–	–	$0.285 \pm 0.015$
H-010	0.29	0.28	0.30	0.28	0.30	–	$0.290 \pm 0.010$

**Table A.3:** Thickness of the adhesive layer of series H specimens

	Specimens	$t_{avg}$ [mm]
Group 1	G-001, G-002, G-004, G-005, G-006, G-008, G-009, G-010	0.270
Group 2	G-003, G-007	0.170
Group 3	H-001	0.085
Group 4	H-002, H-003, H-005, H-006, H-008	0.177
Group 5	H-004, H-007, H-009, H-010	0.282

**Table A.4:** Groups used for specimen selection

	$L$ [mm]	$w$ [mm]	$t$ [mm]	$t_{adh}$ [mm]
G-002	272	24.97	12.40	0.282
G-006	272	25.11	12.44	0.292
G-008	272	24.99	12.41	0.285
G-010	272	25.04	12.40	0.290
H-002	271	25.05	12.36	0.225
H-003	272	25.06	12.36	0.190
H-006	270	25.05	12.36	0.227
H-008	271	25.03	12.39	0.227

**Table A.5:** Summary of the specimens employed in tests

ably different values of the thickness. On the other hand the thickness should also vary as little as possible between A and B, not to invalidate the assumption of constant thickness. For instance let us consider specimen G-003: its average thickness is 0.28 mm at point A and it decreases to 0.16 mm at the midline, a notable relative variation. An average value of the thickness can be easily estimated by the arithmetical mean of these values, giving 0.22 mm as a result. In addition to that, though this specimen belongs to series G, that should theoretically exhibit the thickest adhesive, the found values fall in the same range as most specimens from series H. This simple example shows the need to choose the specimens properly before testing. Proceeding with a similar reasoning as in the proposed example the two batches have been subdivided into smaller groups, each of which with its own average thickness (obtained simply by an arithmetical mean and neglecting the error of each specimen). The groups are shown in Table A.4.

By a comparison between the groups we can notice that a significant difference in the thickness exists between the specimens belonging to Group 1 and Group 4, thus making them a good choice. Data of the specimens which

have been used for fatigue testing (averaged when needed) are summarized in Table [A.5](#).



# Bibliography

- [1] ASTM. “ASTM Standard D5528-01: standard test method for mode I interlaminar fracture toughness of unidirectional fiber-reinforced polymer matrix composites”. West Conshohocken (PA), 2007.
- [2] H. Jiang. “Cohesive Zone Model for Carbon Nanotube Adhesive Simulation and Fracture/Fatigue Crack Growth”. University of Akron, 2010.
- [3] K. Park and G.H. Paulino. “Cohesive Zone Models: A Critical Review of Traction-Separation Relationships Across Fracture Surfaces”. In: *Applied Mechanics Reviews* 64(6), 060802 (2011).
- [4] J.A. Pascoe, R.C. Alderliesten, and R. Benedictus. “On the relationship between disbond growth and the release of strain energy”. In: *Engineering Fracture Mechanics* 133, 1-13 (2014).
- [5] J.A. Pascoe, R.C. Alderliesten, and R. Benedictus. “Towards Understanding Fatigue Disbond Growth via Cyclic Strain Energy”. 20th European conference on fracture. Proc Mater Sci 2014; 3(ECF-20):610-5.
- [6] D. Roylance. “Introduction to Fracture Mechanics”. Department of Materials Science and Engineering, Massachusetts Institute of Technology, 2001.
- [7] Dassault Systèmes. *Abaqus Analysis User’s Manual, Version 6.7*. URL: <http://www.egr.msu.edu/software/abaqus/Documentation/docs/v6.7/books/usb/default.htm?startat=pt06ch26s05alm40.html>.